

The magnetic field strengths of accreting millisecond pulsars

Dipankar Mukherjee^{1*}, Peter Bult², Michiel van der Klis² and Dipankar Bhattacharya³

¹*Research School of Astronomy and Astrophysics, The Australian National University, Canberra, ACT 2611, Australia*

²*Anton Pannekoek Institute, University of Amsterdam, Science Park 904, 1098 XH Amsterdam, The Netherlands*

³*Inter University Centre for Astronomy and Astrophysics, Post Bag 4, Pune 411007, India.*

2 March 2024

ABSTRACT

In this work we have estimated upper and lower limits to the strength of the magnetic dipole moment of all 14 accreting millisecond X-ray pulsars observed with the *Rossi X-ray Timing Explorer (RXTE)*. For each source we searched the archival *RXTE* data for the highest and lowest flux levels with a significant detection of pulsations. We assume these flux levels to correspond to the closest and farthest location of the inner edge of the accretion disk at which channelled accretion takes place. By estimating the accretion rate from the observed luminosity at these two flux levels, we place upper and lower limits on the magnetic dipole moment of the neutron star, using assumptions from standard magnetospheric accretion theory. Finally, we discuss how our field strength estimates can be further improved as more information on these pulsars is obtained.

Key words: pulsars: general – stars:neutron – X-rays:binaries – stars: magnetic fields

1 INTRODUCTION

Magnetic field strengths of neutron stars span a wide range; from $\gtrsim 10^{14}$ G in magnetars via $\sim 10^{12}$ G in most radio pulsars down to $\sim 10^8$ G in millisecond pulsars. The millisecond pulsars are thought to attain their fast spin and low magnetic field strength through accretion in low-mass X-ray binaries (Alpar et al. 1982; Radhakrishnan & Srinivasan 1982; Bailes 1989). The discovery of accreting millisecond X-ray pulsars (AMXPs, Wijnands & van der Klis 1998) and transitional millisecond pulsars (Papitto et al. 2013b) has lent strong support to this picture. However, a full understanding of the evolutionary scenario will only emerge through the comparison of both spin and magnetic field distributions of the LMXB neutron stars with those of transitional and millisecond radio pulsars. In this paper we undertake the task of estimating the magnetic field strengths of the AMXP population in a consistent approach.

Magnetic field strengths of neutron stars are estimated in a variety of ways. For non-accreting radio pulsars the field strengths are inferred from the spin-down rate due to electromagnetic torque (e.g. Ostriker & Gunn 1969; Beskin et al. 1984; Spitkovsky 2006). For anomalous X-ray pulsars, rough estimates of the field can also be obtained by modelling the non-thermal X-ray spectra with cyclotron and magnetic

Compton scattering processes in the magnetosphere (Güver et al. 2007, 2008).

For accreting systems, the available methods for estimating the field strength are less robust. X-ray pulsars with high surface field strengths ($\gtrsim 10^{12}$ G), may show resonant electron cyclotron lines in their X-ray spectra, which give an estimate of the local field strength in the line formation region (Caballero & Wilms 2012). However, the location of this region is unclear, resulting in uncertainties in the measured dipole moment. For lower surface field strengths, as for AMXPs, cyclotron resonances move out of the X-ray band, leaving only indirect methods for estimating the field strength.

In this paper we estimate the magnetic field strength of AMXPs using X-ray observations obtained with the *Rossi X-ray Timing Explorer (RXTE)*. We assume that the accretion disk is truncated at an inner radius that depends on the magnetic field strength and the accretion rate. Below the truncation radius the disk is disrupted and matter is forced to move along the magnetic field to the magnetic polar caps of the neutron star, creating localised hotspots responsible for X-ray pulsations (see, e.g., Poutanen & Beloborodov 2006). The detection of X-ray pulsations is taken to imply ongoing magnetically channelled accretion onto the neutron star, such that the highest and lowest flux levels with detected pulsations identify the range of luminosities (and hence accretion rates) over which such accretion occurs. Assuming a disk-magnetic field interaction model,

* E-mail: dipankar.mukherjee@anu.edu.au

these measurements can then be used to constrain the surface dipole field strength of the neutron star.

To calculate the dipole moment from the set of flux levels, we consider the Ghosh & Lamb (1978, 1979) model of disk-magnetic field interaction, applied in a manner akin to that adopted by Psaltis & Chakrabarty (1999). We assume magnetically channelled to mean that the disk truncation radius is outside the neutron star surface, but smaller than the co-rotation radius (Pringle & Rees 1972; Illarionov & Sunyaev 1975), keeping in mind that these radii only set an approximate scale for the system. The accretion disk may not extend all the way down to the neutron star surface and channelled accretion may persist for a disk truncated outside the co-rotation radius (Spruit & Taam 1993; Rappaport et al. 2004; Bult & van der Klis 2015). How this choice of radii affects our magnetic field strength estimates is discussed in section 4.3.

We plan the paper as follows: in Sec. 2 we review the theory of accretion-disk/magnetic-field interaction, the details of our field strength estimation method and X-ray analysis; in Sec. 3 we describe the outburst history of the considered sources and the results of our analysis; in Sec. 4, we discuss the uncertainties in our method and how they affect our results; and finally in Sec. 5 we compare our results with previous estimates of the magnetic field strength. Technical details of the timing and spectral analysis are presented in Appendix A and B respectively.

2 MAGNETIC FIELD STRENGTH ESTIMATION METHOD

2.1 Theory of disk-stellar magnetic field interaction

For accretion in a steady state, the inner truncation radius depends on the balance between magnetic and material stresses. Equating the torque from the magnetic stresses and the angular momentum flux (Ghosh & Lamb 1979; Rappaport et al. 2004)¹, one finds that

$$\frac{d(\dot{M}r^2\Omega_K)}{dr} = B_\phi B_p r^2, \quad (1)$$

where \dot{M} is the accretion rate, r the distance from the compact object, Ω_K the Keplerian angular velocity at r , and B_p and B_ϕ the respective poloidal and toroidal components of the magnetic field. For simplicity we calculate the torques at the truncation radius considering the spin axis to be aligned to the magnetic dipole, with the accretion disk being perpendicular to both axes. The toroidal field component is produced due to shearing of the poloidal fields. Its strength is an uncertain parameter as it depends on various poorly understood processes like turbulent diffusion and magnetic reconnection (Wang 1995). Another uncertain quantity is the radial extent of the accretion disk, Δr , over which matter couples to the stellar magnetic field and is channelled away from the disk. By expressing these uncertain quantities with the boundary layer parameter, $\gamma_B = (B_\phi/B_p)(\Delta r/r_t)$, the

truncation radius r_t can be related to the poloidal magnetic field and hence the dipole moment as

$$B_p = \gamma_B^{-1/2} (GM\dot{M}^2)^{1/4} r_t^{-5/4}, \quad (2)$$

where G is the gravitational constant and M the neutron star mass. Assuming a dipolar magnetic field, $B_p(r) = \mu/r^3$, with μ the magnetic dipole moment, the truncation radius is given as

$$r_t = \gamma_B^{2/7} \left(\frac{\mu^4}{GM\dot{M}^2} \right)^{1/7}. \quad (3)$$

The truncation radius is related to the classical Alfvén radius r_A as $r_t = \gamma_B^{2/7} 2^{1/7} r_A$, where

$$\left. \begin{aligned} r_A &= (2G)^{-1/7} B_s^{4/7} M^{-1/7} \dot{M}^{-2/7} R_s^{12/7} \\ &= 31 \text{ km} \left(\frac{B_s}{10^8 \text{ G}} \right)^{4/7} \left(\frac{R_s}{10 \text{ km}} \right)^{12/7} \\ &\times \left(\frac{\dot{M}}{10^{16} \text{ g s}^{-1}} \right)^{-2/7} \left(\frac{M}{1.4 M_\odot} \right)^{-1/7} \end{aligned} \right\} \quad (4)$$

Here $B_s = \mu/R_s^3$ is the magnetic field strength at the equator and R_s the neutron star radius.

At higher accretion rates the truncation radius will be closer to the neutron star surface. In this work we assume the disk to extend all the way down to the neutron star surface at the highest accretion rate. At the lowest accretion rate we assume the truncation radius to be at the co-rotation radius. Both radii are rough approximations as true behaviour of the accretion disk truncation radius depends on uncertain aspects like disk/field coupling and the local magnetic field topology (Kulkarni & Romanova 2013; D’Angelo & Spruit 2012, 2010; Romanova et al. 2008). We discuss the effects and limitations of these assumptions in Sec. 4.3.

By identifying the highest and the lowest accretion rates with ongoing magnetic channelling (confirmed by the detection of pulsations), we estimate the magnetic field as outlined below.

For all sources we adopt the canonical neutron star mass of $M = 1.4 M_\odot$ and radius $R_s = 10 \text{ km}$. The value of γ_B is highly uncertain and depends on where the accretion disk is truncated. To be conservative we take γ_B to vary between a wide range of 0.01 – 1 (Psaltis & Chakrabarty 1999).

(i) **Lower limit on μ :** At the highest accretion rates, to observe pulsations, the magnetic field must be at least high enough to truncate the accretion disk at or above the neutron star surface. Thus by setting $r_t = R_s$ we obtain the lower limit on the dipole moment as

$$\mu_{\min} = \gamma_B^{-1/2} (GM)^{1/4} \dot{M}_{\max}^{1/2} R_s^{7/4}, \quad (5)$$

We assume the mass accretion rate can be estimated from the bolometric luminosity as $L = GM\dot{M}/R_s$, and estimate L from the observed luminosity in the X-ray band by applying a bolometric correction factor ($L = \epsilon_{\text{bol}} L_X$). The typical reported values of the bolometric correction factor have a range of $\epsilon_{\text{bol}} \sim 1 - 2$ (Gilfanov et al. 1998; Galloway et al. 2002; Campana et al. 2003; Migliari & Fender 2006; Casella et al. 2008; Galloway et al. 2008). The mass accretion rate

¹ Viscous stresses at the truncation point have been ignored

then follows as

$$\dot{M} = 10^{16} \text{ g s}^{-1} \left(\frac{\epsilon_{\text{bol}} L_X}{1.87 \times 10^{36} \text{ erg s}^{-1}} \right) \times \left(\frac{M}{1.4 M_\odot} \right)^{-1} \left(\frac{R_s}{10 \text{ km}} \right). \quad (6)$$

Expressing the X-ray luminosity in terms of the observed X-ray flux and the assumed distance ($L_X = 4\pi d^2 F$), we obtain the lower limit on the magnetic moment

$$\mu_{\text{min}} = 9.36 \times 10^{24} \text{ G cm}^{-3} \left(\frac{\gamma_B}{1} \right)^{-1/2} \left(\frac{\epsilon_{\text{bol}}}{1} \right)^{1/2} \times \left(\frac{F_{\text{max}}}{10^{-10} \text{ erg cm}^{-2} \text{ s}^{-1}} \right)^{1/2} \left(\frac{d}{10 \text{ kpc}} \right) \times \left(\frac{M}{1.4 M_\odot} \right)^{-1/4} \left(\frac{R_s}{10 \text{ km}} \right)^{9/4}, \quad (7)$$

where F_{max} is the highest observed X-ray flux with pulsation and we adopted the boundary values of γ_B and ϵ_{bol} that give the lowest magnetic moment. For a detailed discussion of these assumptions we again refer to sec. 4.

(ii) **Upper limit on μ :** We assume magnetic channelling to be centrifugally inhibited if the accretion disk is outside the co-rotation radius

$$r_c = \left(\frac{GM}{(2\pi\nu_s)^2} \right)^{1/3}, \quad (8)$$

where ν_s is the spin frequency. We then obtain an upper limit on the dipole moment by setting the truncation radius at the co-rotation radius ($r_t = r_c$) for the lowest accretion rate with detected pulsations

$$\mu_{\text{max}} = \gamma_B^{-1/2} (2\pi)^{-7/6} (GM)^{5/6} \dot{M}_{\text{min}}^{1/2} \nu_s^{-7/6}. \quad (9)$$

By again substituting the expression for the mass accretion rate we obtain the upper limit on the magnetic dipole moment

$$\mu_{\text{max}} = 1.52 \times 10^{27} \text{ G cm}^{-3} \left(\frac{\gamma_B}{0.01} \right)^{-1/2} \left(\frac{\epsilon_{\text{bol}}}{2} \right)^{1/2} \times \left(\frac{F_{\text{min}}}{10^{-11} \text{ erg cm}^{-2} \text{ s}^{-1}} \right)^{1/2} \left(\frac{d}{10 \text{ kpc}} \right) \times \left(\frac{M}{1.4 M_\odot} \right)^{1/3} \left(\frac{R_s}{10 \text{ km}} \right)^{1/2} \left(\frac{\nu_s}{100 \text{ Hz}} \right)^{-7/6}, \quad (10)$$

where F_{min} is the lowest observed X-ray flux with pulsation and we adopted the boundary values of γ_B and ϵ_{bol} that maximize the magnetic moment.

2.2 Data analysis

We analysed all AMXP outbursts observed with *RXTE*. The general structure of our analysis is as follows; for each *RXTE* observation we estimate the Crab normalized X-ray flux and then search for the presence of pulsations. We select the highest and lowest flux observations with detected pulsations, and from spectral analysis measure the source flux. Using these flux measurements and the best distance estimate from literature, we obtain limits on the magnetic dipole moment from eq. 7 and 10. These limits are expressed in terms of the magnetic dipole field strength at the equator ($B_p = \mu/r$), assuming a 10 km radius. The detailed procedure is outlined below.

2.2.1 Timing analysis

We initially estimate the 2–16 keV Crab normalised X-ray flux from the 16-second time-resolution Standard-2 data (see e.g. van Straaten et al. 2003 for details). To search for pulsations we consider the high time resolution GoodXenon or (122 μ s) Event mode data of the same observation, selecting only those events in energy channels 5–37 ($\sim 2 - 16$ keV), which usually provides an optimal signal to noise ratio for the pulsations. The data were barycentred using the FTOOLS task *fbary*, which also applies the *RXTE* fine clock corrections, thus allowing for timing analysis at an absolute precision of $\sim 4\mu$ s (Rots et al. 2004). We then take each ~ 3000 s continuous light curve (as set by the *RXTE* orbit), and fold it on the pulsar ephemeris (see appendix A) to construct a pulse profile. For each profile we measure the amplitude at the fundamental frequency and that of its second harmonic (Hartman et al. 2008).

In standard procedures (see, e.g. Patruno & Watts 2013), a pulsation is usually said to be significant if the measured amplitude exceeds a detection threshold. This threshold is set as the amplitude for which there is only a small probability ϵ that one of the observations in an outburst exceeds it by chance. For observed amplitudes higher than this threshold we have a high confidence $\mathcal{C} = 1 - \epsilon$ that pulsations are detected ($\mathcal{C} = 99.7\%$). We can then consider the flux estimates associated with the significant pulse detections and straightforwardly select the observations of highest and lowest flux.

This approach is very conservative, as it sets a small joint false-alarm probability of detection for the entire outburst, in spite of the fact that we can be certain that pulsation are present in most observations. At the low flux end of the outburst, where the detection significance decreases with the count rate, this may cause us to miss pulsations.

To overcome this issue we first reduce the number of trials by comparing the observed total count rate of an observation with the X-ray background as estimated with the FTOOLS task *pcabackest* (Jahoda et al. 2006). We then set a minimal count-rate threshold and reject all observation for which the pulse amplitude cannot be detected above the noise level assuming the expected source contribution is 100% modulated.

We then select all observations of an outburst that do not have significant pulsations according to the procedure described above. If the pulsar emission is indeed not present in these observations, then the distribution of measured amplitudes and phases should correspond to the expected distribution of random noise, i.e. the phases should be uniform and the squared amplitude should follow a χ^2 -distribution for two degrees of freedom. We compare the distributions using a KS-test, again with a 99.7% confidence level. If the data is not randomly distributed we take out the highest flux observation that has a significant pulse detection at the single trial level and whose phase is consistent with the expectation from the timing model, and iterate until the sample is consistent with being random. The last removed observation is then taken as the lowest observed flux with pulsations. We note that in practice the sensitivity of this iterative approach is limited by the small number of observations in the tail of an outburst and only rarely yields a lower flux pulse detection than through the initial procedure outlined above.

2.2.2 Spectral analysis

For the spectral analysis of selected observations we used HEASOFT version 6.12 and the calibration database (CALDB). Spectra were extracted from the Standard-2 data following the standard procedures outlined in the *RXTE* cookbook². The background was again estimated using the FTOOLS task *pcabackest*. A dead-time correction was applied to the spectra following the prescription in the *RXTE* cookbook³. The spectral fits were done in the 3–20 keV energy range with XSPEC version 12.7.1.

From the measured flux we calculate the 3–20 keV X-ray luminosity and convert to the bolometric luminosity by multiplying with the correction factor ϵ_{bol} . The bolometric correction factor for a source depends on its spectral state, which in turn varies with accretion rate. The typical range of the bolometric correction factor is reported to be $\epsilon_{\text{bol}} \sim 1-2$ (Gilfanov et al. 1998; Galloway et al. 2002; Campana et al. 2003; Migliari & Fender 2006; Casella et al. 2008; Galloway et al. 2008). To be conservative we use $\epsilon_{\text{bol}} = 1$ when calculating μ_{min} and $\epsilon_{\text{bol}} = 2$ when calculating μ_{max} .

For many of the AMXPs considered here, there is considerable contaminating background emission in the observed X-ray flux, for instance from Galactic ridge emission. To estimate the background contamination, we also measured the bolometric luminosity for an observation in the tail of the outburst, where pulsations were not present and the light curve has asymptotically levelled off to a constant value. We assume that in such a state, accretion has ceased and the observed flux is purely due to background emission.

The details of the spectral fit parameters for different sources are presented in Appendix. B.

3 RESULTS

In the following sections we present the magnetic field estimates we obtained from the timing and spectral analysis of all AMXPs observed with *RXTE*. For each source we briefly describe the outburst history, distance estimates and discuss specific details of our analysis. All results are summarized in Tables 1 and 2.

3.1 Swift J1756.9–2508

Swift J1756.9–2508 was first discovered with *Swift* in June 2007 (Krimm et al. 2007a,b), and 182 Hz pulsations were found with follow-up *RXTE* observations (Markwardt et al. 2007). The source showed a second outburst in July 2009 (Patruno et al. 2009b, 2010a).

We find both the highest and lowest flux with pulsations to occur during the 2009 outburst (Fig. 1), with a detection of pulsation for the outburst peak luminosity at MJD 55026.1 and lowest flux detection on MJD 55032.5, just before the light curve decays to the background level. The background contribution was measured from the last observation on MJD 55037.0.

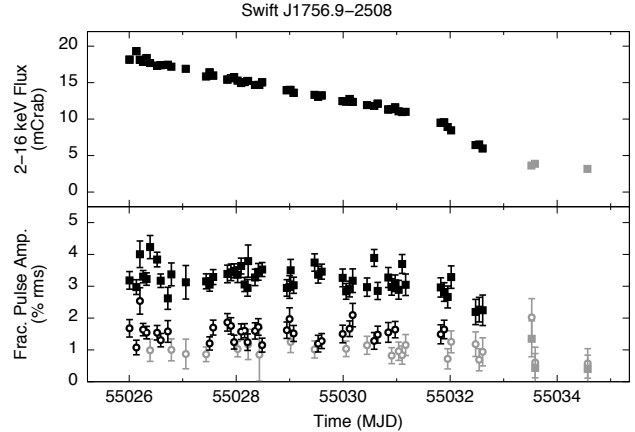


Figure 1. Upper panel: Light curve of the 2009 outburst of Swift J1756.9–2508 normalised to mCrab. Lower panel: pulse amplitude of the fundamental (squares) and the second harmonic (open circles). The observations with significant detection (with 99.7% confidence limit) of pulsation are marked with black, observations without a significant detection of pulsations are shown in grey.

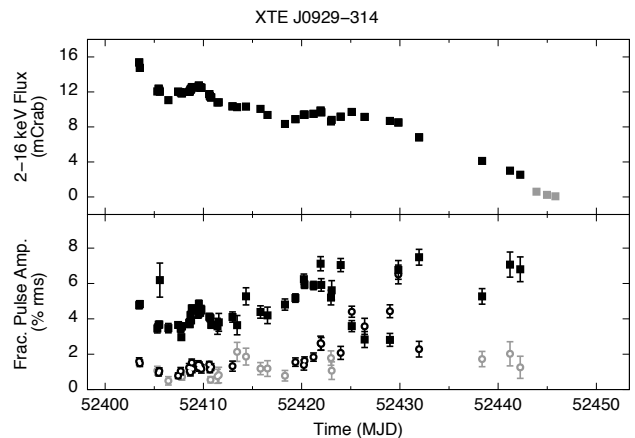


Figure 2. Light curve of the 2002 outburst of XTE J0929–314. Legends are same as in Fig. 1.

The distance to the source is not known, but considering its close proximity to the galactic centre (Krimm et al. 2007a), we assume a distance of 8 kpc. We then obtain a magnetic field range of $1.8 \times 10^7 \text{ G} < B < 2.4 \times 10^9 \text{ G}$.

3.2 XTE J0929–314

XTE J0929–314 was discovered in April 2002 with *RXTE*, and the 185 Hz pulsations were immediately detected (Remillard 2002; Remillard et al. 2002). The source has been detected in outburst only once, with the light curve shown in Fig. 2.

XTE J0929–314 is significantly away from the galactic plane (galactic coordinates: $260.1^\circ, 14.2^\circ$) and shows a low neutral hydrogen column density ($\sim 7.6 \times 10^{20} \text{ cm}^{-2}$, Juett et al. 2003). The background contribution for this source is therefore negligibly low, and indeed could not be measured as the non-pulsating observations at the end of the outburst, which have too few counts to constrain the spectrum.

² http://heasarc.nasa.gov/docs/xte/recipes/cook_book.html

³ http://heasarc.gsfc.nasa.gov/docs/xte/recipes/pca_deadtime.html

Table 1. Flux range with pulsations of the analysed AMXPs in order of ascending spin frequency.

| No | Name | Spin (Hz) | Maximum flux | | Minimum flux | | Background flux | |
|----|--------------------|--------------|--------------|--|--------------|--|-----------------|--|
| | | | MJD | Flux ($\text{erg cm}^{-2} \text{s}^{-1}$) | MJD | Flux ($\text{erg cm}^{-2} \text{s}^{-1}$) | MJD | Flux ($\text{erg cm}^{-2} \text{s}^{-1}$) |
| 1 | Swift J1756.9–2508 | 182 | 55026.1 | 6.30×10^{-10} | 55032.5 | 1.99×10^{-10} | 55037.0 | 4.07×10^{-11} |
| 2 | XTE J0929–314 | 185 | 52403.5 | 4.42×10^{-10} | 52442.3 | 6.64×10^{-11} | – | – |
| 3 | XTE J1807.4–294 | 191 | 52697.6 | 8.19×10^{-10} | 52808.7 | 3.51×10^{-10} | 52816.8 | 7.25×10^{-11} |
| 4 | NGC 6440 X-2 | 206 | 55073.1 | 2.62×10^{-10} | 55873.3 | 3.36×10^{-11} | 55823.2 | 1.34×10^{-11} |
| 5 | IGR J17511–3057 | 245 | 55088.8 | 8.65×10^{-10} | 55124.0 | 1.00×10^{-10} | 55118.2 | 6.96×10^{-11} |
| 6 | XTE J1814–338 | 314 | 52814.3 | 4.41×10^{-10} | 52844.1 | 6.00×10^{-11} | 52852.9 | 1.00×10^{-12} |
| 7 | HETE J1900.1–2455 | 377 | 53559.5 | 1.15×10^{-9} | 53573.8 | 3.84×10^{-10} | – | – |
| 8 | SAX J1808.4–3658 | 401 | 52563.2 | 1.85×10^{-9} | 50936.8 | 2.82×10^{-11} | 50935.1 | 1.21×10^{-11} |
| 9 | IGR J17498–2921 | 401 | 55789.6 | 1.13×10^{-9} | 55818.3 | 4.44×10^{-10} | 55826.4 | 4.23×10^{-10} |
| 10 | XTE J1751–305 | 435 | 52368.7 | 1.50×10^{-9} | 52377.5 | 3.97×10^{-10} | 52380.7 | 6.51×10^{-11} |
| 11 | SAX J1748.9–2021 | 442 | 55222.5 | 4.13×10^{-9} | 52198.3 | 2.96×10^{-9} | 55254.6 | 1.88×10^{-11} |
| 12 | Swift J1749.4–2807 | 518 | 55300.9 | 5.24×10^{-10} | 55306.7 | 2.67×10^{-10} | 55307.7 | 2.41×10^{-10} |
| 13 | Aql X-1 | 550 | 50882.0 | 8.74×10^{-9} | 50882.0 | 8.74×10^{-9} | 50939.8 | 1.34×10^{-11} |
| 14 | IGR J00291+5934 | 599 | 53342.3 | 9.70×10^{-10} | 53352.9 | 1.09×10^{-10} | 53359.5 | 5.76×10^{-11} |

For each source we give the minimum and maximum flux with pulsations. We also give the corresponding 3–20 keV background flux used in calculating the magnetic dipole moment and the MJD of the analysed observations.

Table 2. The magnetic field strength estimates (equatorial surface field) of all considered AMXPs.

| No | Name | Spin (Hz) | Distance (kpc) | Background corrected | B_{\min} (10^8 G) | B_{\max} (10^8 G) | $B_{K,\max}$ (10^8 G) | B_L (10^8 G) | ref. |
|----|--------------------|--------------|-------------------|-------------------------|---------------------------|---------------------------|-----------------------------|----------------------|------|
| 1 | Swift J1756.9–2508 | 182 | 8 | y | 0.18 | 24.1 | 7.2 | 0.4 – 9 | a |
| 2 | XTE J0929–314 | 185 | 6 | n | 0.12 | 11.5 | 3.4 | – | |
| 3 | XTE J1807.4–294 | 191 | 4.4 | n | 0.11 | 18.6 | 5.4 | – | |
| 4 | NGC 6440 X-2 | 206 | 8.2 | y | 0.12 | 7.6 | 2.1 | – | |
| 5 | IGR J17511–3057 | 245 | 7 | n | 0.19 | 11.8 | 3.1 | – | |
| 6 | XTE J1814–338 | 314 | 8 | y | 0.16 | 7.8 | 1.8 | $\lesssim 5 - 10$ | b |
| 7 | HETE J1900.1–2455 | 377 | 5 | n | 0.16 | 10.0 | 2.1 | – | |
| 8 | SAX J1808.4–3658 | 401 | 3.5 | n | 0.14 | 1.77 | 0.36 | 0.7 – 1.5 | c |
| 9 | IGR J17498–2921 | 401 | 8 | n | 0.20 | 16.0 | 3.2 | – | |
| 10 | XTE J1751–305 | 435 | 7 | y | 0.25 | 11.0 | 2.1 | 3.3 – 4.7 | d |
| 11 | SAX J1748.9–2021 | 442 | 8.2 | y | 0.49 | 37.8 | 7.2 | – | |
| 12 | Swift J1749.4–2807 | 518 | 6.7 | n | 0.11 | 7.7 | 1.4 | – | |
| 13 | Aql X-1 | 550 | 5 | y | 0.44 | 30.7 | 5.3 | $\lesssim 9$ | e |
| 14 | IGR J00291+5934 | 599 | 3 | n | 0.085 | 1.9 | 0.31 | 1.5 – 2.0 | f |

(a) Patruno et al. (2010a), (b) Watts et al. (2008); Papitto et al. (2007); Haskell & Patruno (2011), (c) Patruno et al. (2012), (d) Riggio et al. (2011a), (e) Di Salvo & Burderi (2003a), (f) Patruno (2010).

The values B_{\min} and B_{\max} correspond to field strengths estimated using eq. 7 and eq. 10. The values B_K are upper limits to the field strength computed using eq. 12 following the modified expression of truncation radius as obtained by Kulkarni & Romanova (2013) (see Sec. 4.3). B_L are field strength measurements from literature (see references). The background correction column indicates if the background estimate (Table 1) was used when calculating the upper limit on the magnetic field estimate (see, e.g., Sec. 3.3).

There are no good estimates of the distance to the source, with the only constraint claiming $d \gtrsim 6$ kpc based on estimates of average accretion rate Galloway et al. (2002). Using this distance we obtain a magnetic field range of $1.2 \times 10^7 \text{ G} < B < 1.2 \times 10^9 \text{ G}$.

3.3 XTE J1807.4–294

XTE J1807.4–294 was discovered in February 2003 (Markwardt et al. 2003) and the 191 Hz pulsations were immediately found with the *RXTE* observations. The source has been in outburst only once. We find the highest and

lowest flux with pulsations to occur on MJD 52697.6 and MJD 52808.7, respectively (Fig. 3).

We measured the background contribution on MJD 52816.8, but note that this background level is similar to the lowest flux with pulsations, such that the uncertainty in the background estimation is larger than the apparent source contribution. To be conservative we calculate the upper limit to the magnetic moment without adjusting for the background. This implies that we take the low flux observation as an upper limit to the true lowest flux at which pulsations are present. If the presence of pulsations can be established at a lower flux level, the upper

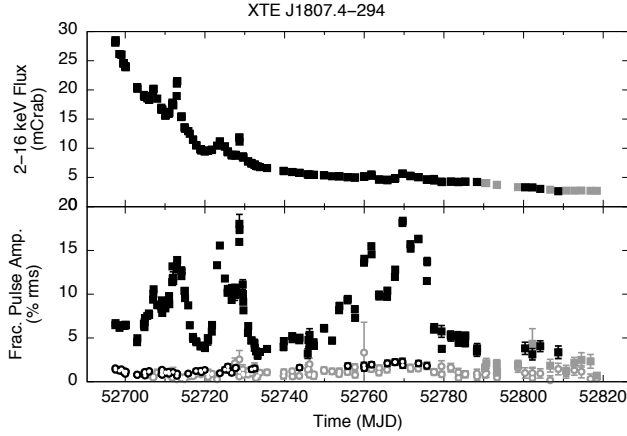


Figure 3. Light curve of the 2003 outburst of XTE J1807.4-294. Legends are same as in Fig. 1.

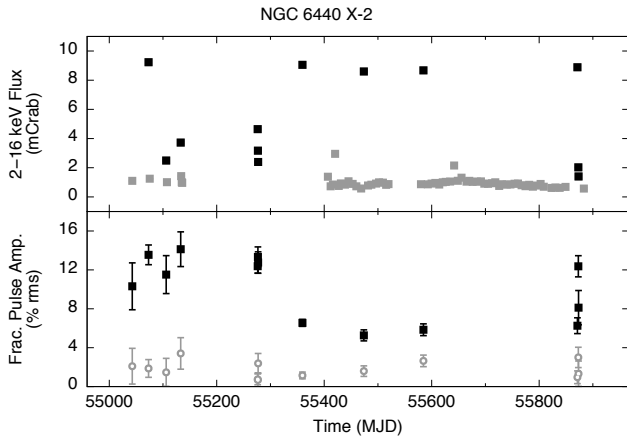


Figure 4. Light curve of NGC 6440 X-2 from July, 2009 to November, 2011. Legends are same as in Fig. 1.

limit will decrease, thus tightening the allowed magnetic field range.

There are no well defined estimates for the distance to this source. Some authors assume the source is near the galactic centre (Falanga et al. 2005a; Campana et al. 2003), and take the distance to be ~ 8 kpc. Others, however, estimate the distance at ~ 4.4 kpc (Riggio et al. 2008), by comparing the observed flux to the accretion rate inferred from the pulse timing analysis. Lacking a more robust estimation of the distance, we adopt a distance of 4.4 kpc. We then arrive at a magnetic field range estimate of $1.1 \times 10^7 \text{ G} < B < 1.9 \times 10^9 \text{ G}$.

3.4 NGC 6440 X-2

NGC 6440 X-2 is located in the globular cluster NGC 6440 and was detected serendipitously with *Chandra* in July 2009 (Heinke & Budac 2009; Heinke et al. 2010). Pulsations at 206 Hz were discovered from subsequent *RXTE* observations (Altamirano et al. 2009, 2010a).

The outburst behaviour of NGC 6440 X-2 is atypical, as it shows brief outbursts of a few days with a recurrence time as short as one month (see Fig. 4). Due to the high-cadence

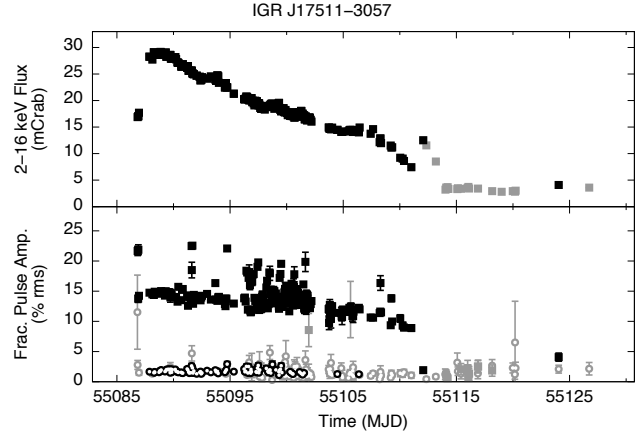


Figure 5. Light curve of the 2009 outburst of IGR J17511-3057. Legends are same as in Fig. 1.

monitoring of this globular cluster, the background level is well established between MJD 55700–55850. We estimate the background flux on MJD 55823.2.

The distance to the cluster NGC 6440 is well constrained to $d = 8.2$ kpc (Valenti et al. 2007), and gives a magnetic field range of $1.2 \times 10^7 \text{ G} < B < 7.6 \times 10^8 \text{ G}$.

3.5 IGR J17511-3057

IGR J17511-3057 was discovered with *INTEGRAL* in September 2009 (Baldovin et al. 2009), with subsequent *RXTE* observations discovering 245 Hz pulsations (Markwardt et al. 2009).

The outburst light curve shows a notable flare after MJD 55110 (Fig. 5) which is attributed to simultaneous activity of XTE J1751-305 (Falanga et al. 2011). Pulsations are observed throughout the outburst, and reoccur on MJD 55124.0, some 10 days after the source appears to have reached the background level. We select this observation as the lowest flux observation with pulsations, and select the observation on MJD 55118.2 for the background flux. Since the flux difference between these observations is very small (Table 1, we consider the low flux observation to be background dominated and, like in Sec. 3.3, neglect the background measurement in calculating the upper limit on the magnetic moment to obtain a more conservative estimate of the magnetic field strength.

The distance to this source is estimated at $\lesssim 7$ kpc, derived by assuming the type I X-ray bursts are Eddington limited (Altamirano et al. 2010b; Papitto et al. 2010). Adopting this distance we obtain a magnetic field range of $1.9 \times 10^7 \text{ G} < B < 1.2 \times 10^9 \text{ G}$.

3.6 XTE J1814-338

XTE J1814-338 was discovered in June 2003 with *RXTE* and immediately recognized as a 314 Hz pulsar (Markwardt & Swank 2003). It has been detected in outburst only once, and shows pulsations throughout its outburst (Fig. 6).

We measured the background flux from the observation on MJD 52852.9, one of the last *RXTE* observations of the outburst.

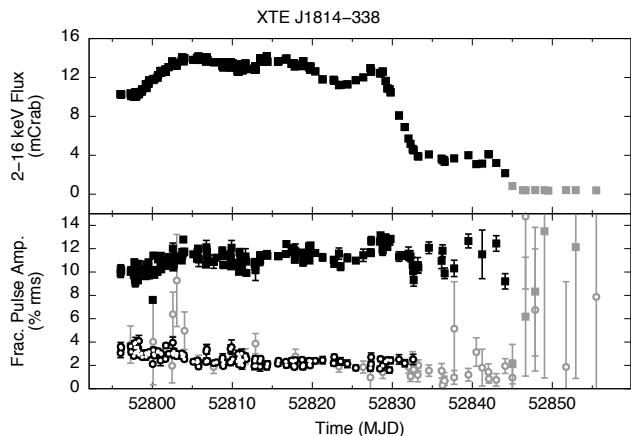


Figure 6. Light curve of the 2003 outburst of XTE J1814-338. Legends are same as in Fig. 1.

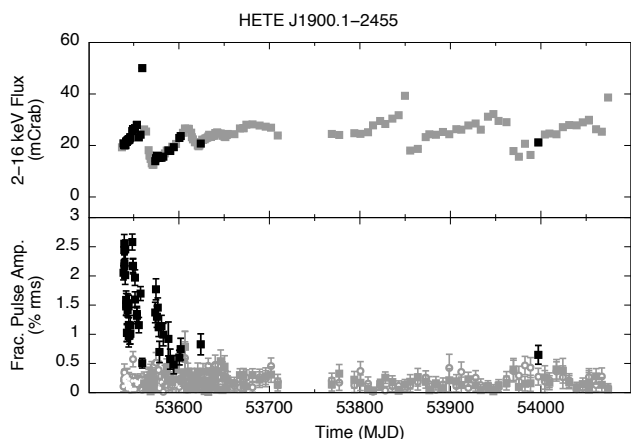


Figure 7. Light curve of HETE J1900.1-2455 from June 2005 to January 2007. Legends are same as in Fig. 1. Note that there are additional pulse detections beyond ~ 54000 , however, these are tentative (Patruno 2012) and do not change the measured flux range.

The distance to the source is estimated at $\lesssim 8$ kpc, by assuming the measured luminosity during the type I X-ray burst is Eddington limited (Strohmayer et al. 2003). The resulting magnetic field range is $1.6 \times 10^7 \text{ G} < B < 7.8 \times 10^8 \text{ G}$.

3.7 HETE J1900.1-2455

HETE J1900.1-2455 was discovered through a bright type I X-ray burst observed with the *High Energy Transient Explorer 2* (HETE-2) in June 2005 (Vanderspek et al. 2005) and 377 Hz pulsations were observed with *RXTE* quickly thereafter (Morgan et al. 2005; Kaaret et al. 2006). Unlike the other AMXPs, which show outbursts that last for weeks to months, HETE J1900.1-2455 has been active since discovery and is yet to return to quiescence. Persistent pulsations have been reported to occur during the first 20 days of the outburst, after which only intermittent pulsations have been seen (Patruno 2012).

We have analysed all archival *RXTE* observations

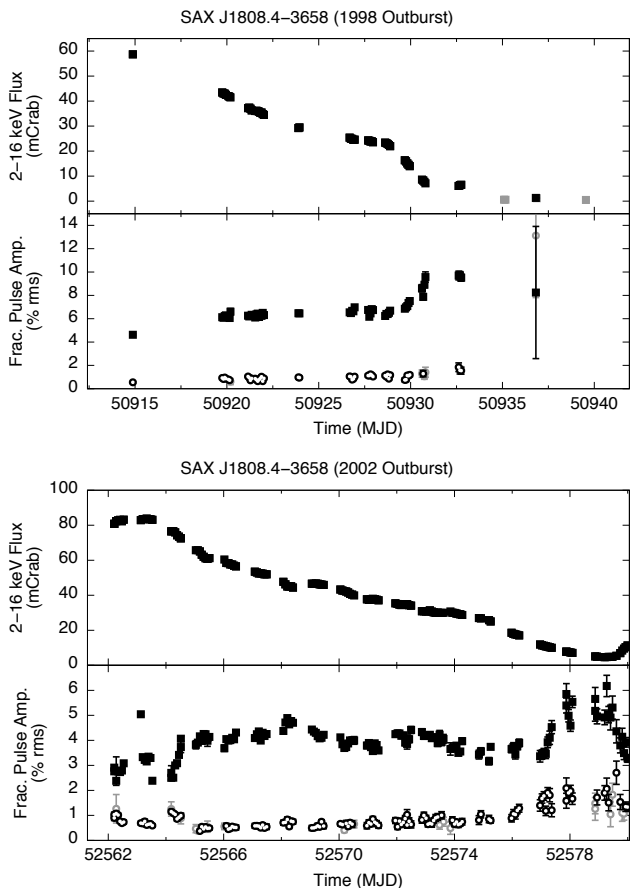


Figure 8. Light curve of the 1998 and 2002 outbursts of SAX J1808.4-3658. Legends are same as in Fig. 1.

of this source and find that the observations of highest and lowest flux with pulsations are on MJD 53559.5 and MJD 53573.8, respectively.

Since the source has shown continuous activity since its discovery, there is no observation during quiescence from which the background flux can be estimated. However, as the source is well away from the galactic centre (galactic coordinates: $l = 11.3^\circ, b = -12.9^\circ$), the background flux is expected to be comparatively small. We therefore neglect the background contribution for this source, noting again that this leads us to slightly overestimate the source flux, which yields a less stringent constraint on μ_{\max} .

The distance to the source is taken to be $d \sim 5$ kpc, based on photospheric radius expansion of a type I X-ray burst (Kawai & Suzuki 2005). The magnetic field range obtained is $1.6 \times 10^7 \text{ G} < B < 1.0 \times 10^9 \text{ G}$.

3.8 SAX J1808.4-3658

SAX J1808.4-3658 was discovered with *BeppoSax* in 1996 (in 't Zand et al. 1998) and the detection of 401 Hz pulsations in 1998 with *RXTE* made it the first known AMXP (Wijnands & van der Klis 1998). SAX J1808.4-3658 has been observed in outbursts with *RXTE* six times.

We find the highest flux with pulsations to be in the 2002 outburst on MJD 52563.2 and the lowest flux with pulsations in the 1998 outburst on MJD 50936.8. The low-

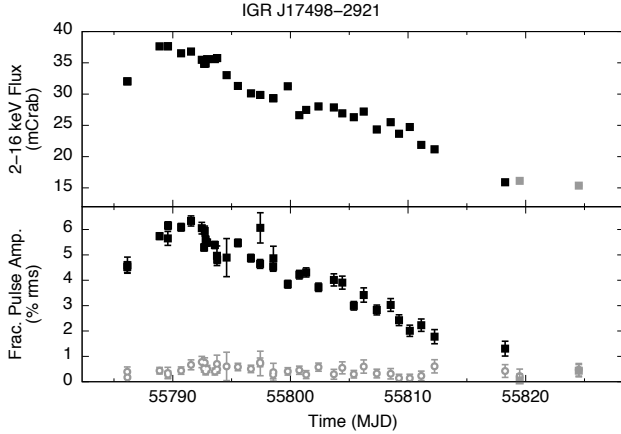


Figure 9. Light curve of the 2011 outburst of IGR J17498–2921. Legends are same as in Fig. 1.

est flux with pulsations is observed toward the end of the 1998 outburst (Fig. 8). Although the flux of this observation is only slightly higher than that of the background observations, the pulse detection is very significant and yields a phase that is consistent with the timing model of this outburst. If pulsations are still present at the same amplitude in the other low flux observations, we would not be able to detect them due to the low count rate. We therefore consider the low flux observation with pulsations to be background dominated.

The distance to SAX J1808.4–3658 is $d = 3.5$ kpc, and was derived from photospheric radius expansion in type I X-ray bursts Galloway & Cumming (2006). With this distance we obtain a magnetic field range of $1.4 \times 10^7 \text{ G} < B < 1.8 \times 10^8 \text{ G}$.

3.9 IGR J17498–2921

IGR J17498–2921 was discovered in August 2011 with *INTEGRAL* (Gibaud et al. 2011), following which pulsations at 401 Hz were reported by Papitto et al. (2011b). The light curve of this outburst is shown in Fig. 9.

Since the source is close to the galactic centre (galactic coordinates: $l = 0.16^\circ$, $b = -1^\circ$), the observations have a large X-ray background contamination, with the lowest observed flux with pulsations again background dominated.

The distance to IGR J17498–2921 is estimated at ~ 8 kpc, based on photospheric radius expansion during a type I X-ray burst (Falanga et al. 2012). We then find a magnetic field range of $2.0 \times 10^7 \text{ G} < B < 1.6 \times 10^9 \text{ G}$.

3.10 XTE J1751–305

XTE J1751–305 and its 435 Hz pulsations were discovered with *RXTE* in April 2002 (Markwardt et al. 2002a). A brief second outburst was detected in 2009 (Markwardt et al. 2009), which was coincident with on-going activity of IGR J17511–3057 in the same field of view. Since *RXTE* is not an imaging detector, the flux contribution of these two sources cannot be separated, so we restricted our analysis to the 2002 outburst of XTE J1751–305 only.

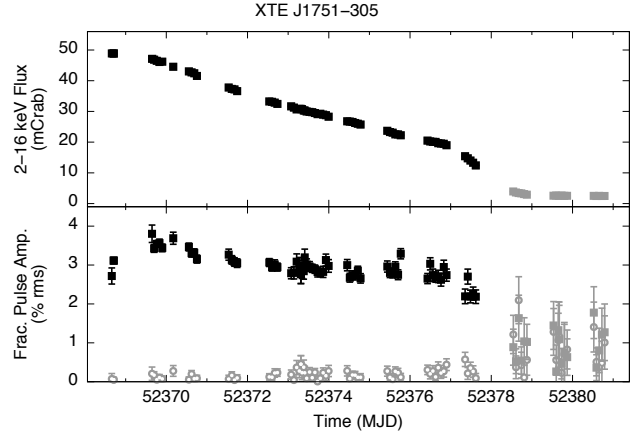


Figure 10. Light curve of the 2002 outburst of XTE J751–305. Legends are same as in Fig. 1.

We estimate the background from the last *RXTE* observation on MJD 52380.7, when the pulsations were no longer detected (see Fig. 10).

The distance to this source is not well-defined. Markwardt et al. (2002a) constrain the distance to $\gtrsim 7$ kpc by equating predicted mass transfer rates (Rappaport et al. 1983; King et al. 1997) to values inferred from X-ray observations. Papitto et al. (2008) instead compare the spin-frequency derivative to models for angular momentum exchange (Rappaport et al. 2004), and so constrain the distance to $6.7 - 8.5$ kpc. For our analysis, we take a distance of 7 kpc, which results in a magnetic field range of $2.5 \times 10^7 \text{ G} < B < 1.1 \times 10^9 \text{ G}$.

3.11 SAX J1748.9–2021

SAX J1748.9–2021 is located in the globular cluster NGC 6440 (in 't Zand et al. 1999), and was observed in outburst by *RXTE* in 1998, 2001, 2005 and 2010 (in 't Zand et al. 1999; in 't Zand et al. 2001; Markwardt & Swank 2005; Patruno et al. 2010b). Among these outbursts 442 Hz intermittent pulsations have been detected in 2001, 2005 and 2010 (Gavril et al. 2007; Altamirano et al. 2008; Patruno et al. 2010b).

We find that the highest flux with pulsations occurs during the 2010 outburst on MJD 55222.5, while the lowest flux with pulsations is seen in the 2001 outburst on MJD 52198.3 (light curves shown in Fig. 11).

As the source is associated with a globular cluster, its distance is comparatively well constrained to 8.2 kpc (Valenti et al. 2007). We find a magnetic field range of $4.9 \times 10^7 \text{ G} < B < 3.8 \times 10^9 \text{ G}$.

3.12 Swift J1749.4–2807

Swift J1749.4–2807 was first detected in June 2006 (Schady et al. 2006), but its 518 Hz pulsations were not found until the second outburst in April 2010 (Altamirano et al. 2010c, 2011). We find both the highest and lowest flux with pulsations occur in this second outburst on MJD 55300.9 and 55306.7, respectively.

The source is located close to the galactic centre and

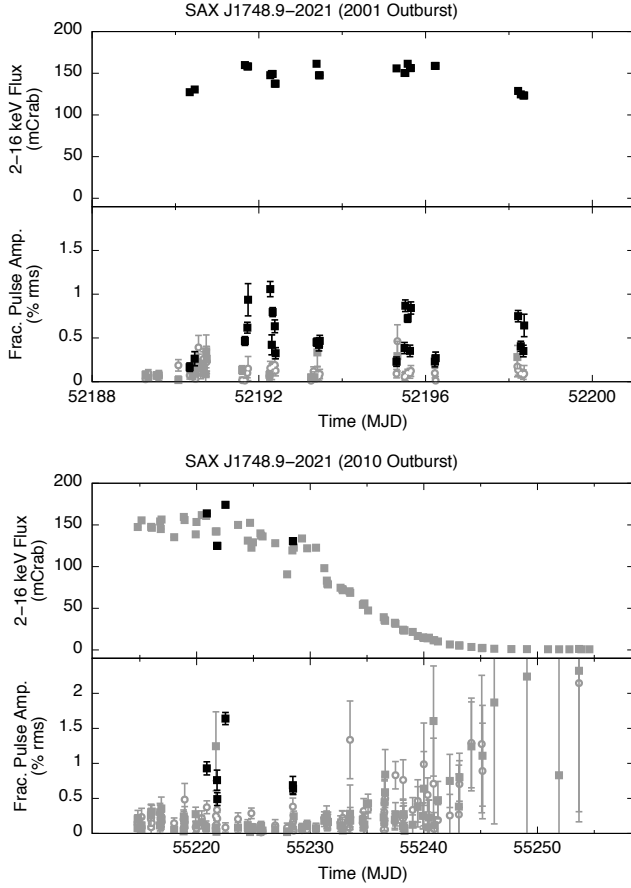


Figure 11. Light curves of the 2001 and 2010 outbursts of SAX J1748.9-2021. Legends are same as in Fig. 1.

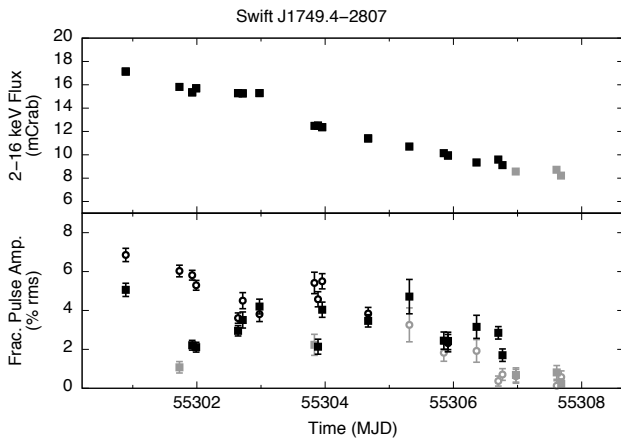


Figure 12. Light curve of the 2010 outburst of Swift J1749.4-2807. Legends are same as in Fig. 1.

has a strong contaminating X-ray background flux. The absence of pulsations (Fig. 12) indicate that the source was no longer accreting for the last three *RXTE* observations ($> \text{MJD } 55307$), which is confirmed by a source non-detection with both *Swift* and *INTEGRAL* (Ferrigno et al. 2011). We therefore use the last *RXTE* observation to measure the background flux. As this background flux is compa-

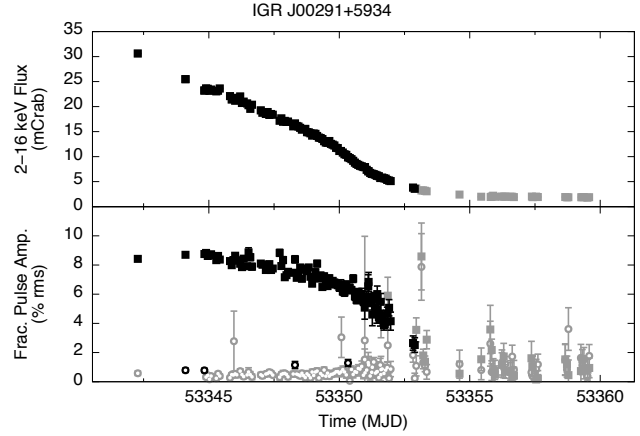


Figure 13. Upper panel: Light curve of the 2004 outburst of IGR J00291+5934. Legends are same as in Fig. 1.

table to the lowest observed flux with pulsations, we cannot confidently estimate the source contribution and to be conservative we again calculate the upper limit on the magnetic field without using the background.

The distance to the source is $d = 6.7 \pm 1.3$ kpc, which was inferred from the luminosity of a suspected type I X-ray burst (Wijnands et al. 2009). Adopting the central value for the distance and the measured flux we obtain a magnetic field range of $1.1 \times 10^7 \text{ G} < B < 7.7 \times 10^8 \text{ G}$.

3.13 Aql X-1

In 18 outbursts across ~ 15 years, Aql X-1 has shown its 550 Hz pulsations only for a single episode of about 150 seconds (Casella et al. 2008; Messenger & Patruno 2014). Hence we cannot measure a flux range for the presence of pulsations for this source. Instead we calculate both lower and upper limits on the magnetic field from the same measured flux, thus obtaining a very conservative estimate of the allowed magnetic field range.

The distance to the source is 4.4 – 5.9 kpc and was obtained from a photospheric radius expansion during a type I X-ray (Jonker & Nelemans 2004). For a distance of 5 kpc and the measured flux we obtain a magnetic field range of $4.4 \times 10^7 \text{ G} < B < 3.1 \times 10^9 \text{ G}$.

3.14 IGR J00291+5934

IGR J00291+5934 was discovered with *INTEGRAL* in December 2004 (Eckert et al. 2004; Shaw et al. 2005) and its 599 Hz pulsations were detected in follow-up *RXTE* observations (Markwardt et al. 2004). Outbursts were detected again in August and September 2008 (Chakrabarty et al. 2008; Lewis et al. 2008). We find both the highest and the lowest flux with pulsations occur in the 2004 outburst.

It is evident from the light curve (Fig. 13) that the source gradually decays to the background level, which is due to an intermediate polar in the same field of view (Falanga et al. 2005b). Because the lowest flux with pulsations is again comparable to the estimated background flux, we assume the low flux observation is background dominated to get a more conservative magnetic field estimate.

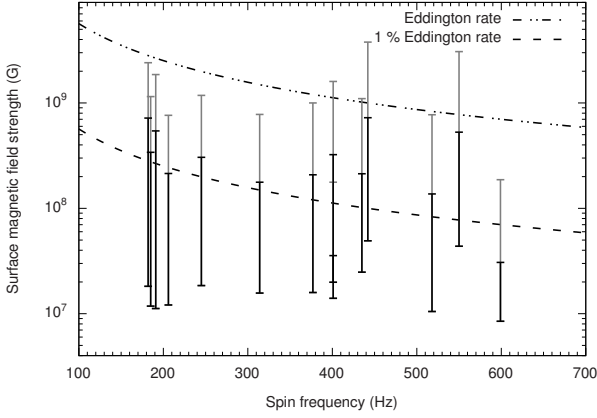


Figure 14. Magnetic field vs spin frequency for AMXPs analysed in this work. The grey lines show the range of estimated field strengths of the sources from Table 2. The black lines represent the revised upper limits following eq. 11 which gives tighter constraints of the field strength estimates. The dashed and dash-dotted curves show the equilibrium spin rate for two different accretion rates.

The distance to IGR J00291+5934 has been estimated in several ways. From the long term average accretion rate, Galloway et al. (2005) constrain the distance to $\lesssim 4$ kpc. Comparing the observed quiescent flux to that of SAX J1808.4–3658, Jonker et al. (2005) estimate the distance to be 2–3.6 kpc. Similar estimates were also obtained by Torres et al. (2008), who report $d = 1.8 - 3.8$ kpc by modeling the light curve. In this work we adopt the central distance of $d = 3$ kpc, which gives a magnetic field range of $8.5 \times 10^6 \text{ G} < B < 1.9 \times 10^8 \text{ G}$.

4 DISCUSSION

In this section we discuss the various sources of uncertainty involved in the magnetic field estimates presented in this work.

4.1 Distance estimates

The largest uncertainties in our field estimates are due to poor constraints on the distance. Errors in the distance affect the luminosity estimates and cause a systematic uncertainty that scales both the upper and lower limit by the same factor ($B_{\min/\max} \propto d$). The sources associated with globular clusters are not greatly affected by this uncertainty as they have well measured distances. Some AMXPs exhibit thermonuclear bursts with photospheric radius expansion, which allows for tight constraints on the distance. For the remaining sources, however the distance measurements are less certain and the resulting systematic uncertainty has a more prominent role. In Table 2 we explicitly report the distances used in calculating the upper and lower limits, such that our estimates can be easily adjusted should a more accurate measure distance be obtained for one of these sources.

4.2 Masses and radii of AMXPs

Currently there are no reliable estimates available for the masses or radii of AMXPs. In calculating the field strengths presented in Table 2 we assumed the neutron stars to be of canonical mass $M \sim 1.4M_{\odot}$ and radius ~ 10 km. However, theoretical calculations of mass-radius relations (e.g. Lattimer & Prakash 2001; Lattimer 2014) predict that both parameters may vary over a wide range of $M \sim 0.2 - 2.9M_{\odot}$ and $R \sim 10 - 15$ km.

For a more massive neutron star of $\sim 2M_{\odot}$ the upper limit on the magnetic dipole moment will increase by $\sim 12.6\%$ ($\mu_{\max} \propto M^{1/3}$), whereas the lower limit will decrease by 8.2% ($\mu_{\min} \propto M^{-1/4}$) from the values reported in Table 2, resulting in a broadening of the estimated range.

For a neutron star of larger radius, e.g. ~ 15 km, the upper limit on the magnetic dipole moment will scale as $\mu_{\max} \propto R^{1/2}$, causing an increase of 22.5% with respect to the values we report. The lower limit to the magnetic dipole moment scales with radius as $\mu_{\min} \propto R^{9/4}$, such that assuming a 15 km radius increases the lower limit by 149%. For a $R = 15$ km neutron star we then find that the allowed range of magnetic field strength moves to higher values and covers a slightly broader range⁴.

4.3 Disk-magnetosphere interaction

In this paper we made the assumption that the neutron star magnetic field is dipolar in nature, which may not be valid. Near the truncation radius the pressure the disk exerts on the magnetosphere can affect the field geometry, and near the neutron star surface this may be further complicated by higher multipole moments that could dominate over the dipole component. We parametrized the effect of the field shape with the factor γ_B (see eq. 3), which we assumed to vary over a wide range of 0.01–1 to account for such uncertainties. This range is consistent with the results of numerical simulations, which suggest the largest range of truncation radii is $r_t \sim (0.5 - 1.2)r_A$ (Zanni & Ferreira 2009; Romanova et al. 2008), implying $\gamma_B \simeq 0.06 - 1.3$.

• Recent MHD simulations (Zanni & Ferreira 2013; Kulkarni & Romanova 2013; Long et al. 2008; Romanova et al. 2008) have confirmed that complex field topologies arise at the inner edge of the disk. Kulkarni & Romanova (2013) show that if the truncation radius is in the range $2.5R_s < r_t < 5R_s$, the non-dipolar field structure results in a modified expression of the truncation radius

$$r_t = 1.06R_s \left(\frac{\mu^4}{GM\dot{M}^2R_s^7} \right)^{1/10} \quad (11)$$

This modification is relevant when estimating the upper limit to the magnetic field, for which we take the disk to be truncated at the co-rotation radius, which normally falls within the range of radii where eq. 11 is applicable. Using

⁴ The field strength range covers more than an order of magnitude, so despite the large fractional change, the absolute shift of the lower limit is smaller than that of the upper limit.

this expression for the truncation radius we obtain a modified boundary layer parameter as

$$\tilde{\gamma}_B = 0.0616 \left(\frac{\nu_s}{100 \text{ Hz}} \right) \left(\frac{M}{1.4 M_\odot} \right)^{-1/2} \left(\frac{R_s}{10 \text{ km}} \right)^{3/2} \quad (12)$$

which, instead of conservatively assuming 0.01, may be used in eq. 10 to obtain a more constraining upper limit on the magnetic dipole moment.

- Near the neutron star surface higher multipole moments of the magnetic field may be stronger than the dipole component. As shown in numerical studies (Long et al. 2007, 2008) such complex non-dipolar field configurations strongly affect the inner accretion geometry, but the effect on γ_B is not well established. If further theoretical considerations can constrain γ_B to a smaller value than our conservative assumption of $\gamma_B = 1$, then this could be used to tighten the lower limit on the magnetic field strength ($B_{\min} \propto \gamma_B^{-1/2}$).

In Fig. 14 we plot the conservative ranges of the surface field strength following the analysis in Sec. 2.1 in grey and present the more constraining estimates based on eq. 12 in black. The dashed lines represent the equilibrium spin (Alfvén radius at co-rotation) for a mean long term accretion rate

$$\begin{aligned} \nu_{\text{eq}} = 441 \text{ Hz} & \left(\frac{B_s}{10^9 \text{ G}} \right)^{-6/7} \left(\frac{R_s}{10 \text{ km}} \right)^{-18/7} \\ & \times \left(\frac{\dot{M}}{\dot{M}_E} \right)^{3/7} \left(\frac{M}{1.4 M_\odot} \right)^{5/7} \end{aligned} \quad (13)$$

where $\dot{M}_E = 1.5 \times 10^{-8} M_\odot \text{ yr}^{-1}$ is the Eddington accretion rate.

- In our analysis we assumed that channelled accretion onto the neutron star can only take place when the disk is truncated inside the co-rotation radius. However, the large range of X-ray luminosities, and accordingly mass accretion rates, observed for AMXPs suggests that mass accretion onto the neutron star might persist even when the inner edge of the disk moves outside the co-rotation radius (see e.g. Rappaport et al. 2004), which indeed appears to be confirmed by observation (Bult & van der Klis 2015).

As pointed out by Spruit & Taam (1993) the inner edge of the disk must have receded to $r_t \sim 1.3 r_c$ before the centrifugal force is strong enough to accelerate matter beyond the escape velocity and thus drive an outflow. If we consider the possibility that accretion may still occur for radii up-to $1.3 r_c$, then we find that the upper limit to the magnetic field strength increases by 58% ($B_{\max} \propto (r_t/r_c)^{7/4}$) at most. The lower limit, being independent of the co-rotation radius, is unaffected.

4.4 Observational sampling

- In order to determine the upper limit to the magnetic field strength we consider the lowest observed flux for which pulsations are significantly detected. However, as the flux decays, the signal-to-noise ratio also decreases, such that the non-detection of pulsations could be due to limited statistics. That is, the pulsations may persist below our detection limit. This concern is particularly relevant to XTE J1807.4–294, IGR J17498–2921, and IGR J17511–3057 in which pulsations are detected at approximately the same flux as the

background level. If pulsations are still present at a very low level, and accretion is ongoing at even lower luminosities, then our estimates for these sources are overly conservative as we are overestimating the upper limit to the magnetic field strength. Since $B_{\max} \propto L^{1/2}$, a future detection of pulsations at a lower luminosity than reported in this work can therefore be used to further constrain the range of magnetic field strengths. This is especially relevant for other X-ray satellites that have better sensitivity and a lower background contamination such as XMM-Newton, or for a future ASTROSAT (Agrawal 2006; Singh 2014) or LOFT (Feroci et al. 2012) mission.

- For the lower limit to the magnetic field strength we use the highest observed flux for which pulsations are detected. As we note in Sec. 2 the pulsations are expected to disappear at high flux when the disk extends to the neutron star surface, yet this is never observed. For all sources the highest observed flux considered always shows pulsations, which implies that the inner edge of the disk never extends down to the neutron star surface. Indeed some of the better sampled AMXPs (e.g. SAX J1808.4–3658 and IGR J00291+5934) show peak luminosities that vary by a factor of 2 between outbursts. If a future outburst reaches a higher peak luminosity than considered in this work, it will increase the lower limit as $B_{\min} \propto L^{1/2}$ and thus further constrain the allowed range of magnetic field strength.

4.5 Luminosity estimates

- To calculate the flux we consider the 3–20 keV X-ray band, which we convert to the bolometric flux by applying a correction factor (Gilfanov et al. 1998; Casella et al. 2008; Galloway et al. 2002; Campana et al. 2003). To be conservative in our estimates of the field strength we used a $\epsilon_{\text{bol}} = 2$ for the upper limit and $\epsilon_{\text{bol}} = 1$ for the lower limit. However, if the correction factor is well constrained then this approach is overly pessimistic. For many accretion powered pulsars the correction factor tends to be within $\sim 10\%$ of 2 (Galloway et al. 2008), such that the error introduced in the magnetic field estimate is only $\sim 2\%$ ($B_{\max} \propto (\epsilon_{\text{bol}}/2)^{1/2}$, $B_{\min} \propto (\epsilon_{\text{bol}}/1)^{1/2}$). If we adopt the same bolometric correction factor for the lower limit also, it we find the our estimates can improve by up-to $\lesssim 30\%$.

- Another source of uncertainty comes from the background contribution to the measured flux. We estimate the background contribution from the *RXTE* observations at the end of an outburst, when the source no longer shows pulsations and has presumably returned to quiescence. If this estimate contains residual source emission, or the background contribution itself is variable, then this approach introduces an error in our field strength limits.

Because the highest observed flux with pulsations is always much higher than the background the lower limit to the magnetic field strength will not be greatly affected by the uncertainty in the background estimate. The lowest observed flux with pulsations, however, is often comparable to the background contribution, so the effect on the upper limit needs to be considered carefully.

For some sources the background flux is sufficiently lower than the minimum pulsating flux (as shown in Table 1) that the effect of the background correction amounts to only a small change in the field estimates (e.g. $\sim 8\%$

for XTE J1814–38, $\sim 12\%$ for Swift J1756.9–2508). For sources where background flux could not be measured (HETE J1900.1–2455 and XTE J0929–314) the error introduced by neglecting the background is expected to similarly be only a few percent.

The remaining sources have a comparatively high background contribution, such that the estimated background flux is a large fraction of the minimum pulsating flux. For these AMXPs we conservatively took the lowest observed flux with pulsations as an upper limit to the real flux at which pulsations and thus accretion stops. We then calculated the upper limit on the magnetic field strength without adjusting for the background. Accounting for the background would lower the source flux estimate by up-to a factor of two, and thus improve our estimates by roughly $\lesssim 40\%$. Further improvement might be achievable with more sensitive instrumentation (as noted in the previous section).

- To convert the observed flux to the source luminosity we assumed an isotropic emission process, however, the flux includes contributions from the hotspot, which may have a significant anisotropy (Poutanen & Beloborodov 2006; Viironen & Poutanen 2004; Poutanen & Gierliński 2003).

The effect of anisotropic emission is not at all clear. The degree of anisotropy of the hotspot emission depends on assumptions of the emission process and can vary by a factor of ~ 2 (Poutanen & Beloborodov 2006). Furthermore, what fraction of the total flux is affected by this will depend on the size, shape and position of the hotspot and is subject to considerable uncertainty. At best this effect applies only to the pulsed component of the emission ($\sim 10\%$) and thus introduces a systematic error in our estimates of only a few percent. At worst most of the observed flux originates from a large hotspot that has a slightly beamed emission pattern. In that case the allowed magnetic field range may show a systematic shift of up-to $\sim 40\%$.

5 COMPARISON WITH PREVIOUS WORKS

In this work we estimated upper and lower limits to the magnetic field strength of all accreting millisecond X-ray pulsars (AMXPs) observed with *RXTE*. We assume that the detection of X-ray pulsations signifies ongoing magnetically channelled accretion. Thus, by associating the range of luminosity for which pulsations are detected with the expected extent of the disk truncation radius, we have constrained the magnetic dipole moment of the neutron star. The obtained equatorial surface magnetic field strengths of the 14 AMXPs analysed are presented in Table 2.

Our magnetic field strength estimates are subject to a number of uncertainties, which were discussed in the previous section. We note that we have chosen most of the uncertain parameters such that we obtained a conservative range for the magnetic moment. If parameters such as γ_B or ϵ_{bol} can be established more accurately, they will tighten the constraints further. Errors in other parameters, such as the distance to the source, introduce a systematic shift in our results. Refinement in the measurement of these parameters would affect both the upper and the lower limits the same way. Similarly, the uncertainties in the estimation of the background fluxes also affect both limits to the magnetic field. If better estimates are available from more sensitive

instruments and also if there are future outbursts with flux ranges wider than those in the current work, the constraints on the magnetic field in Table 2 can be easily updated by correcting the fluxes presented in Table 1 and recomputing the limits to the dipole moment using eq. 7 and eq. 10.

For 5 of the 14 considered AMXPs (Swift J1749.4–2807, IGR J17511–3057, NGC 6440 X-2, XTE J1807.4–294 and IGR J17498–2921) we obtain constraints on the magnetic field strength for the first time. For the other 9 AMXPs field strength estimates have been previously reported. Below we discuss some of the techniques used to obtain those estimates and how they compare with limits we report here.

(i) *Vacuum dipole radiation in quiescence*: For some AMXPs the spin frequency has been measured for successive outbursts that are months or years apart. Measurements of spin-down during the intervening periods of quiescence, can then be used to estimate the magnetic field strength by assuming the spin-down is due to magnetic dipole emission. Such estimates have been obtained for IGR J00291+5934 (Patruno 2010; Hartman et al. 2011), XTE J1751–305 (Riggio et al. 2011a), SAX J1808.4–3658 (Hartman et al. 2008, 2009; Patruno et al. 2012) and Swift J1756.9–2508 (Patruno 2010). While the radio emission associated with magnetic braking has not yet been detected in any of these sources, the recent discovery of millisecond neutron stars pulsating alternately in X-rays and radio (Papitto et al. 2013b; Archibald et al. 2014; Papitto et al. 2015) provides some evidence that this interpretation of measured spin-down is correct.

Our magnetic field strength estimates appear to be systematically lower than those obtained through quiescent spin down, although we note that given the systematic uncertainties discussed in the previous section, the results of these two approaches are roughly consistent.

(ii) *Quiescent luminosity estimates*: For some LMXBs e.g. SAX J1808.4–3658, Aql X-1 (Di Salvo & Burderi 2003b), KS 1731–260 (Burderi et al. 2002) and XTE J0929–314 (Wijnands et al. 2005), limits to the magnetic field strength have been inferred from measurements of the quiescent X-ray luminosity. However, given the very low count rates in the quiescent phase, and a poor understanding of which physical mechanism governs the radiation process, these methods offer less reliable constraints on the dipole moment compared to other approaches. While for Aql X-1 no other independent confirmation of the upper limits exists, the upper limits for SAX J1808.4–3658 and XTE J0929–314 obtained through quiescent luminosity methods are comparable to the upper limits we report here.

(iii) *Accretion induced spin down estimates*: For some systems the magnetic field strength has been estimated by comparing observed rate of spin down during ongoing accretion to theoretical estimates of magnetic torque. For example, for XTE J1814–338 Papitto et al. (2007) assume that observed pulse frequency variations are caused by spin down due to the torque applied by an accretion disk that is truncated near the co-rotation radius. Following theoretical calculations of accretion induced spin down torques (Rappaport et al. 2004), the authors estimate the surface magnetic field to be $\sim 8 \times 10^8$ G, which is comparable our conservative upper limit to the field, and significantly higher than the upper limit we obtain using eq. 12. However, given their simplifying assumptions regarding the magnetic field topol-

ogy at the Alfvén radius, and the considerable uncertainty in interpreting pulse frequency variations as spin variations (Patruno et al. 2009e), accretion induced spin down estimates are less robust than those we obtain.

(iv) *Burst oscillations*: In some accreting pulsars the phase of burst oscillations in type I X-ray bursts is locked to the phase of the accretion powered pulsations (XTE J1814–338 Watts et al. 2008, IGR J17480–2446 Cavecchi et al. 2011). Cavecchi et al. (2011) argue that if this phase-locking is due to magnetic confinement of the flame propagation front, then it would require a field strength of $\gtrsim 5 \times 10^9$ G. Even given the systematic uncertainties that enter in our estimates, such a large magnetic field strength would be difficult to reconcile with the lower upper limit we obtain for XTE J1814–338.

(v) *Spectral state transitions in LMXBs*: In another approach, spectral state transitions have been used to identify the onset of the propeller regime (Matsuoka & Asai 2013; Asai et al. 2013). These authors argue that a spectral change and a fast decline of luminosity towards the end of an outburst indicates the onset of the propeller regime and thus an accretion disk that is truncated at the co-rotation radius. Such spectral state transitions have been investigated for only a handful of LMXBs (e.g. Aql X-1, 4U 1608–52, XTE J1701–462), but give limits on the magnetic field strength of Aql X-1 that are tighter than those we obtained. However, there is no clear evidence that these transitions are indeed caused by a propeller effect. In fact, the observation of similar state transitions in black hole binaries seems to suggest otherwise (Jonker et al. 2004).

To conclude, the magnetic field estimates we obtain agree with most of the other indirect methods to within an order of magnitude. The large uncertainties on many parameters, as well as the uncertainty in the underlying assumptions, introduce a significant spread in the range of field strengths inferred via each approach, with no single technique being more robust than the others. Nonetheless, all alternative methods discussed in this section require that the AMXP be observed during a specific state of its outburst (e.g. during quiescence or a spectral state transition). Since observations of such special states are not available, or may not even exist, for all sources, these methods are not suitable for studying the population. By contrast, the method used in this work applies to any AMXP, making it more reliable for comparing the field strengths of the population and understanding the evolutionary processes which lead to the formation of AMXPs.

6 ACKNOWLEDGEMENTS

We thank Deepto Chakrabarty, Dimitros Psaltis, Alessandro Patruno, Anna Watts and Sushan Konar for constructive suggestions and helpful discussions which improved the content and presentation of this work. We thank Tolga Güver for his careful scrutiny and comments which helped improve the manuscript. DM thanks CSIR India for the junior research fellow grant 09/545(0034)/2009-EMR-I. DM also acknowledges the hospitality of Anton Pannekoek Institute where part of the work was carried out during his visit. PB and MK acknowledge support from the Netherlands Organisation for Scientific Research (NWO). The work has made use

of the public archival data, part of which is taken from observations originally proposed by the following PIs: Duncan Galloway, Diego Altamirano, Jean Swank, Rudy Wijnands and Wei Cui; the rest being Target of opportunity (TOO) observations of source outbursts.

REFERENCES

- Agrawal P. C., 2006, *Advances in Space Research*, 38, 2989
- Alpar M. A., Cheng A. F., Ruderman M. A., Shaham J., 1982, *Nature*, 300, 728
- Altamirano D., Casella P., Patruno A., Wijnands R., van der Klis M., 2008, *ApJ*, 674, L45
- Altamirano D. et al., 2011, *ApJ*, 727, L18
- Altamirano D. et al., 2010a, *ApJ*, 712, L58
- Altamirano D. et al., 2009, *The Astronomer’s Telegram*, 2182, 1
- Altamirano D., Watts A., Linares M., Markwardt C. B., Strohmayer T., Patruno A., 2010b, *MNRAS*, 409, 1136
- Altamirano D. et al., 2010c, *The Astronomer’s Telegram*, 2565, 1
- Archibald A. M. et al., 2014, *ArXiv e-prints*
- Arnaud K. A., 1996, in *Astronomical Society of the Pacific Conference Series*, Vol. 101, *Astronomical Data Analysis Software and Systems V*, Jacoby G. H., Barnes J., eds., p. 17
- Asai K. et al., 2013, *ApJ*, 773, 117
- Bailes M., 1989, *ApJ*, 342, 917
- Baldovin C. et al., 2009, *The Astronomer’s Telegram*, 2196, 1
- Beskin V. S., Gurevich A. V., Istomin I. N., 1984, *Ap&SS*, 102, 301
- Bult P., van der Klis M., 2015, *ApJ*, 798, L29
- Burderi L. et al., 2002, *ApJ*, 574, 930
- Caballero I., Wilms J., 2012, *MmSAI*, 83, 230
- Cackett E. M., Altamirano D., Patruno A., Miller J. M., Reynolds M., Linares M., Wijnands R., 2009, *ApJ*, 694, L21
- Campana S., Ravasio M., Israel G. L., Mangano V., Belloni T., 2003, *ApJ*, 594, L39
- Casella P., Altamirano D., Patruno A., Wijnands R., van der Klis M., 2008, *ApJ*, 674, L41
- Cavecchi Y. et al., 2011, *ApJ*, 740, L8
- Chakrabarty D., Markwardt C. B., Linares M., Jonker P. G., 2011, *The Astronomer’s Telegram*, 3606, 1
- Chakrabarty D., Swank J. H., Markwardt C. B., Smith E., 2008, *The Astronomer’s Telegram*, 1660, 1
- D’Angelo C. R., Spruit H. C., 2010, *MNRAS*, 406, 1208
- D’Angelo C. R., Spruit H. C., 2012, *MNRAS*, 420, 416
- Di Salvo T., Burderi L., 2003a, *A&A*, 397, 723
- Di Salvo T., Burderi L., 2003b, *A&A*, 397, 723
- Eckert D., Walter R., Kretschmar P., Mas-Hesse M., Palumbo G. G. C., Roques J.-P., Ubertini P., Winkler C., 2004, *The Astronomer’s Telegram*, 352, 1
- Falanga M. et al., 2005a, *A&A*, 436, 647
- Falanga M. et al., 2005b, *A&A*, 444, 15
- Falanga M. et al., 2011, *A&A*, 529, A68
- Falanga M., Kuiper L., Poutanen J., Galloway D. K., Bozzo E., Goldwurm A., Hermsen W., Stella L., 2012, *A&A*, 545, A26
- Feroci M. et al., 2012, *Experimental Astronomy*, 34, 415

- Ferrigno C. et al., 2011, *A&A*, 525, A48
- Fox D. B., 2005, *The Astronomer's Telegram*, 526, 1
- Galloway D. K., Chakrabarty D., Morgan E. H., Remillard R. A., 2002, *ApJ*, 576, L137
- Galloway D. K., Cumming A., 2006, *ApJ*, 652, 559
- Galloway D. K., Markwardt C. B., Morgan E. H., Chakrabarty D., Strohmayer T. E., 2005, *ApJ*, 622, L45
- Galloway D. K., Muno M. P., Hartman J. M., Psaltis D., Chakrabarty D., 2008, *ApJS*, 179, 360
- Gavriil F. P., Strohmayer T. E., Swank J. H., Markwardt C. B., 2007, *ApJ*, 669, L29
- Ghosh P., Lamb F. K., 1978, *ApJ*, 223, L83
- Ghosh P., Lamb F. K., 1979, *ApJ*, 232, 259
- Gibaud L. et al., 2011, *The Astronomer's Telegram*, 3551, 1
- Gierliński M., Poutanen J., 2005, *MNRAS*, 359, 1261
- Gilfanov M., Revnivtsev M., Sunyaev R., Churazov E., 1998, *A&A*, 338, L83
- Güver T., Özel F., Göğüş E., Kouveliotou C., 2007, *ApJ*, 667, L73
- Güver T., Özel F., Göğüş E., 2008, *ApJ*, 675, 1499
- Harris W. E., 1996, *AJ*, 112, 1487
- Hartman J. M., Galloway D. K., Chakrabarty D., 2011, *ApJ*, 726, 26
- Hartman J. M. et al., 2008, *ApJ*, 675, 1468
- Hartman J. M., Patruno A., Chakrabarty D., Markwardt C. B., Morgan E. H., van der Klis M., Wijnands R., 2009, *ApJ*, 702, 1673
- Haskell B., Patruno A., 2011, *ApJ*, 738, L14
- Heinke C. O. et al., 2010, *ApJ*, 714, 894
- Heinke C. O., Budac S. A., 2009, *The Astronomer's Telegram*, 2139, 1
- Iacolina M. N., Burgay M., Burderi L., Possenti A., di Salvo T., 2009, *A&A*, 497, 445
- Illarionov A. F., Sunyaev R. A., 1975, *A&A*, 39, 185
- in 't Zand J. J. M., Heise J., Muller J. M., Bazzano A., Cocchi M., Natalucci L., Ubertini P., 1998, *A&A*, 331, L25
- in 't Zand J. J. M. et al., 1999, *A&A*, 345, 100
- in't Zand J. J. M., van Kerkwijk M. H., Pooley D., Verbunt F., Wijnands R., Lewin W. H. G., 2001, *ApJ*, 563, L41
- Jahoda K., Markwardt C. B., Radeva Y., Rots A. H., Stark M. J., Swank J. H., Strohmayer T. E., Zhang W., 2006, *ApJS*, 163, 401
- Jonker P. G., Campana S., Steeghs D., Torres M. A. P., Galloway D. K., Markwardt C. B., Chakrabarty D., Swank J., 2005, *MNRAS*, 361, 511
- Jonker P. G., Gallo E., Dhawan V., Rupen M., Fender R. P., Dubus G., 2004, *MNRAS*, 351, 1359
- Jonker P. G., Nelemans G., 2004, *MNRAS*, 354, 355
- Juett A. M., Galloway D. K., Chakrabarty D., 2003, *ApJ*, 587, 754
- Kaaret P., Morgan E. H., Vanderspek R., Tomsick J. A., 2006, *ApJ*, 638, 963
- Kawai N., Suzuki M., 2005, *The Astronomer's Telegram*, 534, 1
- King A. R., Kolb U., Szuszkiewicz E., 1997, *ApJ*, 488, 89
- Krauss M. I. et al., 2005a, *ApJ*, 627, 910
- Krauss M. I. et al., 2005b, *ApJ*, 627, 910
- Krimm H. A. et al., 2007a, *The Astronomer's Telegram*, 1105, 1
- Krimm H. A. et al., 2007b, *ApJ*, 668, L147
- Kulkarni A. K., Romanova M. M., 2013, *MNRAS*, 433, 3048
- Lattimer J. M., 2014, *General Relativity and Gravitation*, 46, 1713
- Lattimer J. M., Prakash M., 2001, *ApJ*, 550, 426
- Lewis F. ., Linares M., Russell D. M., Wijnands R., Roche P., 2008, *The Astronomer's Telegram*, 1726, 1
- Long M., Romanova M. M., Lovelace R. V. E., 2007, *MNRAS*, 374, 436
- Long M., Romanova M. M., Lovelace R. V. E., 2008, *MNRAS*, 386, 1274
- Markwardt C. B., Altamirano D., Strohmayer T. E., Swank J. H., 2009, *The Astronomer's Telegram*, 2237, 1
- Markwardt C. B., Dobrzycki A., 2002, *IAU Circ.*, 7876, 2
- Markwardt C. B., Krimm H. A., Swank J. H., 2007, *The Astronomer's Telegram*, 1108, 1
- Markwardt C. B., Smith E., Swank J. H., 2003, *The Astronomer's Telegram*, 122, 1
- Markwardt C. B., Strohmayer T. E., 2010, *ApJ*, 717, L149
- Markwardt C. B., Swank J. H., 2003, *IAU Circ.*, 8144, 1
- Markwardt C. B., Swank J. H., 2005, *The Astronomer's Telegram*, 495, 1
- Markwardt C. B., Swank J. H., Strohmayer T. E., 2004, *The Astronomer's Telegram*, 353, 1
- Markwardt C. B., Swank J. H., Strohmayer T. E., in 't Zand J. J. M., Marshall F. E., 2002a, *ApJ*, 575, L21
- Markwardt C. B., Swank J. H., Strohmayer T. E., in 't Zand J. J. M., Marshall F. E., 2002b, *ApJ*, 575, L21
- Matsuoka M., Asai K., 2013, *PASJ*, 65, 26
- Messenger C., Patruno A., 2014, *ArXiv e-prints*
- Migliari S., Fender R. P., 2006, *MNRAS*, 366, 79
- Miller J. M. et al., 2003, *ApJ*, 583, L99
- Morgan E., Kaaret P., Vanderspek R., 2005, *The Astronomer's Telegram*, 523, 1
- Nowak M. et al., 2009, in *Chandra's First Decade of Discovery*, Wolk S., Fruscione A., Swartz D., eds.
- Ostriker J. P., Gunn J. E., 1969, *ApJ*, 157, 1395
- Paizis A., Nowak M. A., Rodriguez J., Wilms J., Chaty S., Del Santo M., Ubertini P., 2012, *ApJ*, 755, 52
- Paizis A., Nowak M. A., Wilms J., Courvoisier T. J.-L., Ebisawa K., Rodriguez J., Ubertini P., 2005, *A&A*, 444, 357
- Papitto A. et al., 2011a, *A&A*, 535, L4
- Papitto A. et al., 2013a, *MNRAS*, 429, 3411
- Papitto A., de Martino D., Belloni T. M., Burgay M., Pelizzoni A., Possenti A., Torres D. F., 2015, *MNRAS*, 449, L26
- Papitto A., di Salvo T., Burderi L., Menna M. T., Lavagetto G., Riggio A., 2007, *MNRAS*, 375, 971
- Papitto A., Di Salvo T., D'Ai A., Iaria R., Burderi L., Riggio A., Menna M. T., Robba N. R., 2009, *A&A*, 493, L39
- Papitto A., Ferrigno C., Bozzo E., Gibaud L., Burderi L., di Salvo T., Riggio A., 2011b, *The Astronomer's Telegram*, 3556, 1
- Papitto A. et al., 2013b, *Nature*, 501, 517
- Papitto A., Menna M. T., Burderi L., di Salvo T., Riggio A., 2008, *MNRAS*, 383, 411
- Papitto A., Riggio A., di Salvo T., Burderi L., D'Ai A., Iaria R., Bozzo E., Menna M. T., 2010, *MNRAS*, 407, 2575
- Patruno A., 2010, *ApJ*, 722, 909
- Patruno A., 2012, *ApJ*, 753, L12
- Patruno A., Altamirano D., Hessels J. W. T., Casella P.,

- Wijnands R., van der Klis M., 2009a, *ApJ*, 690, 1856
- Patruno A., Altamirano D., Messenger C., 2010a, *MNRAS*, 403, 1426
- Patruno A. et al., 2010b, *The Astronomer's Telegram*, 2407, 1
- Patruno A., Bult P., Gopakumar A., Hartman J. M., Wijnands R., van der Klis M., Chakrabarty D., 2012, *ApJ*, 746, L27
- Patruno A., D'Angelo C., 2013, *ApJ*, 771, 94
- Patruno A., Maitra D., Curran P. A., D'Angelo C., Fridriksson J. K., Russell D. M., Middleton M., Wijnands R., 2015, *ArXiv e-prints*
- Patruno A., Markwardt C. B., Strohmayer T. E., Swank J. H., Smith S. E., Pereira D., 2009b, *The Astronomer's Telegram*, 2130, 1
- Patruno A., Rea N., Altamirano D., Linares M., Wijnands R., van der Klis M., 2009c, *MNRAS*, 396, L51
- Patruno A., Watts A., Klein Wolt M., Wijnands R., van der Klis M., 2009d, *ApJ*, 707, 1296
- Patruno A., Watts A. L., 2013, in *Timing neutron stars: pulsations, oscillations and explosions*, T. Belloni, M. Méndez, C.M. Zhang, ed., *ASSL: Springer*
- Patruno A., Wijnands R., van der Klis M., 2009e, *ApJ*, 698, L60
- Poutanen J., Beloborodov A. M., 2006, *MNRAS*, 373, 836
- Poutanen J., Gierliński M., 2003, *MNRAS*, 343, 1301
- Pringle J. E., Rees M. J., 1972, *A&A*, 21, 1
- Psaltis D., Chakrabarty D., 1999, *ApJ*, 521, 332
- Radhakrishnan V., Srinivasan G., 1982, *Current Science*, 51, 1096
- Rappaport S., Verbunt F., Joss P. C., 1983, *ApJ*, 275, 713
- Rappaport S. A., Fregeau J. M., Spruit H., 2004, *ApJ*, 606, 436
- Remillard R. A., 2002, *IAU Circ.*, 7888, 2
- Remillard R. A., Swank J., Strohmayer T., 2002, *IAU Circ.*, 7893, 1
- Riggio A., Burderi L., di Salvo T., Papitto A., D'Ai A., Iaria R., Menna M. T., 2011a, *A&A*, 531, A140
- Riggio A., Di Salvo T., Burderi L., Menna M. T., Papitto A., Iaria R., Lavagetto G., 2008, *ApJ*, 678, 1273
- Riggio A., Papitto A., Burderi L., di Salvo T., Bachetti M., Iaria R., D'Ai A., Menna M. T., 2011b, *A&A*, 526, A95
- Romanova M. M., Kulkarni A. K., Lovelace R. V. E., 2008, *ApJ*, 673, L171
- Rots A. H., Jahoda K., Lyne A. G., 2004, *ApJ*, 605, L129
- Rupen M. P., Dhawan V., Mioduszewski A. J., 2004, *The Astronomer's Telegram*, 364, 1
- Schady P., Beardmore A. P., Marshall F. E., Palmer D. M., Rol E., Sato G., 2006, *GRB Coordinates Network*, 5200, 1
- Shaw S. E. et al., 2005, *A&A*, 432, L13
- Singh K. P. e. a., 2014, in *Proceedings of the SPIE*, Hidayat B., Feast M. W., eds., Vol. 9144, p. id91441S
- Spitkovsky A., 2006, *ApJ*, 648, L51
- Spruit H. C., Taam R. E., 1993, *ApJ*, 402, 593
- Strohmayer T. E., Markwardt C. B., Swank J. H., in't Zand J., 2003, *ApJ*, 596, L67
- Torres M. A. P. et al., 2008, *ApJ*, 672, 1079
- Torres M. A. P., Madej O., Jonker P. G., Steeghs D., Greiss S., Morrell N., Roth M., 2011, *The Astronomer's Telegram*, 3638, 1
- Valenti E., Ferraro F. R., Origlia L., 2007, *AJ*, 133, 1287
- van Straaten S., van der Klis M., Méndez M., 2003, *ApJ*, 596, 1155
- Vanderspek R., Morgan E., Crew G., Graziani C., Suzuki M., 2005, *The Astronomer's Telegram*, 516, 1
- Viironen K., Poutanen J., 2004, *A&A*, 426, 985
- Wang Y.-M., 1995, *ApJ*, 449, L153
- Watts A. L., Krishnan B., Bildsten L., Schutz B. F., 2008, *MNRAS*, 389, 839
- Wijnands R., Homan J., Heinke C. O., Miller J. M., Lewin W. H. G., 2005, *ApJ*, 619, 492
- Wijnands R., Rol E., Cackett E., Starling R. L. C., Remillard R. A., 2009, *MNRAS*, 393, 126
- Wijnands R., van der Klis M., 1998, *Nature*, 394, 344
- Wilms J., Allen A., McCray R., 2000, *ApJ*, 542, 914
- Zanni C., Ferreira J., 2009, *A&A*, 508, 1117
- Zanni C., Ferreira J., 2013, *A&A*, 550, A99
- Zdziarski A. A., Johnson W. N., Magdziarz P., 1996, *MNRAS*, 283, 193
- Życki P. T., Done C., Smith D. A., 1999, *MNRAS*, 309, 561

Table A1. Adopted T_{asc} values for the outbursts of NGC 6440 X-2.

| NGC 6440 X-2 | |
|--------------|------------------|
| Outburst | T_{asc} |
| Outburst 1 | 55042.817 |
| Outburst 2 | 55073.034 |
| Outburst 3 | 55106.012 |
| Outburst 4 | 55132.907 |
| Outburst 5 | 55276.625 |
| Outburst 6 | 55359.470 |
| Outburst 7 | 55473.854 |
| Outburst 8 | 55584.714 |
| Outburst 9 | 55871.231 |

APPENDIX A: DETAILS OF THE TIMING ANALYSIS

A1 Swift J1756.9–2508:

The two outbursts of Swift J1756.9–2508 were observed with *RXTE* under program IDs P92050 & P93065 (2007) and P94065 (2009). We barycenter this data using the best known coordinates of Krimm et al. (2007b). For the timing solution we adopt the ephemeris of Patruno et al. (2010a).

A2 XTE J0929–314:

We correct the *RXTE* data (program ID P70096) to the Solar system barycenter using the Chandra source position of Juett et al. (2003). The data was folded using the timing solution of Iacolina et al. (2009).

A3 XTE J1807.4–294:

The *RXTE* data of the outburst of XTE J1807.4–294 is given by program IDs P70134 and P80(145/419). We use the Chandra coordinates of Markwardt et al. (2003) to barycenter the data. We use the system ephemeris of Riggio et al. (2008) to fold the data.

A4 NGC 6440 X-2:

The nine short outbursts of NGC 6440 X-2 that were observed with *RXTE* are given by program IDs P94044, P94315 and P95040 (Patruno & D’Angelo 2013). We correct the data to the Solar System barycenter using the Chandra position of Heinke et al. (2010). The timing solution for the first outburst is given by Altamirano et al. (2010a). This timing solution is also used the later outbursts, but with the locally optimized time of ascending node values given in Table A1.

A5 IGR J17511–3057:

The *RXTE* data of the 2009 outburst of IGR J17511–3057 is given by program ID P940(41/42). We barycenter the data using the Chandra position given by Nowak et al. (2009). The timing solution of this source is given by Riggio et al. (2011b).

A6 XTE J1814–338:

The *RXTE* data of XTE J1814–338 is given by program IDs P80(138/145/418) and P92054. The optical position used to barycenter the data is given by Krauss et al. (2005a) and the timing solution is taken from Papitto et al. (2007).

A7 HETE J1900.1–2455:

The source HETE J1900.1–2455 has a long history of activity and thus its *RXTE* data is spread over many program IDs: P910(15/57/59), P91432, P92049, P93(030/451), P940(28/30), P95030 and P96030. For source coordinates we use the optical position of Fox (2005). The timing solution is given by Patruno (2012).

A8 SAX J1808.4–3658:

The *RXTE* program IDs for SAX J1808.4–3658 are given by P30411 (1998), P40035 (2000), P70080 (2002), P91056 & P91418 (2005), P93027 & P93417 (2008) and P96027 (2011). When considering the outbursts of SAX J1808.4–3658 we exclude the prolonged outburst tail which represents an unusual disk state (Patruno et al. 2009d, 2015), so the outburst of 2000 is entirely omitted from the analysis. Source coordinates for barycentering are taken from Hartman et al. (2008). For the ephemeris we adopt the solutions of Hartman et al. (2008, 2009) and Patruno et al. (2012) for the respective outbursts of 1998, 2002 and 2005; 2008; and 2011.

A9 IGR J17498–2921:

RXTE data for IGR J17498–2921 is given by program ID P96435. For the source position we adopt the Chandra coordinates of Chakrabarty et al. (2011). The timing solution is given by Papitto et al. (2011a).

A10 XTE J1751–305:

We only analyze the *RXTE* data of the 2002 outburst (see main text for details) which is given by programs P70131 and P70134. To barycenter the data we use the Chandra position of Markwardt & Dobrzycki (2002). For the orbital ephemeris we use the timing solution of Markwardt et al. (2002b).

A11 SAX J1748.9–2021:

The *RXTE* data of SAX J1748.9–2021 is given by programs P30425, P60035 & P60084 (2001), P91050 (2005) and P94315 (2010). We use the Chandra position of in’t Zand et al. (2001) for barycentering the data. The timing solution of Patruno et al. (2009a) was used to fold the data of the 1998, 2001 and 2005 outbursts and that of Patruno et al. (2010b) for the 2010 outburst.

A12 Swift J1749.4–2807:

We use the data of *RXTE* program P95085. For barycentering we adopt the X-ray coordinates of Wijnands et al. (2009), obtained with XMM-Newton. We use the ephemeris of Altamirano et al. (2011) to fold the data.

A13 IGR J00291+5934:

We use *RXTE* data from programs P90052 and P90425 for the 2004 outburst and program P93013 and P93435 for the 2008 outburst. We use radio coordinates of Rupen et al. (2004) to barycenter the data. The timing solution of Patruno (2010) was used to fold the data.

APPENDIX B: DETAILS OF THE SPECTRAL ANALYSIS

For the spectral analysis we extracted the data of all Xenon layers of PCU2, and for observations with a poor signal to noise ratio we combined data from all active PCUs. Due to poor signal to noise some spectral fits at low flux have a reduced- χ^2 of much less than 1. As our work does not focus on obtaining the most accurate spectral model, but rather on measuring the flux, our final results will not be significantly affected by the model uncertainty of these fits.

Our analysis of the *RXTE/PCA* data was performed for the 3 – 20 keV energy range using XSPEC version 12.7.1. The galactic absorption was modelled with the *TBABS* model (Wilms et al. 2000). Since *RXTE* instruments cannot properly constrain the galactic absorption due to neutral hydrogen in the lower energy range, we fix N_H to values obtained from literature. The errors quoted are for a 95% confidence limit.

B1 Swift J1756.9–2508:

For ObsIDs 94065-02-01-05 (high flux with pulsations, HF) and 94065-06-02-03 (low flux with pulsations, LF) data were extracted from PCU2 whereas for 94065-06-03-02 (background estimate, BE), data from PCU 0, 2 and 4 were combined for the spectral analysis. The HF and BE spectra were fit with a simple absorbed power-law model *XSPEC* (Arnaud 1996). The LF spectrum was fit with a power-law continuum and a thermal black body component. The hydrogen column density accounting for galactic absorption was fixed to $N_H = 5.4 \times 10^{20} \text{ cm}^{-2}$ (Krimm et al. 2007b). A Gaussian emission component centred at ~ 6.5 keV (width fixed to 10^{-3} keV) was required to obtain statistically acceptable fits. The results of the spectral analysis are presented in Table B1.

B2 XTE J0929–314:

For ObsID 70096-03-02-00 (HF) data were extracted from PCUs 0, 2, 3 & 4 whereas for 70096-03-14-00 (LF) they were extracted from PCUs 0, 2, 4. The spectra were fit with a power-law continuum and thermal blackbody component. The hydrogen column density was fixed to $N_H = 7.6 \times 10^{20} \text{ cm}^{-2}$ (Juett et al. 2003). The results are presented in Table B2.

B3 XTE J1807.4–294:

For ObsIDs 70134-09-02-01 (HF) and 80145-01-17-02 (LF) the data were extracted from PCU2 whereas for 80419-01-01-01 (BE) data were extracted from PCUs 0, 2 and 3. The

HF spectrum was fit with a power-law continuum and thermal blackbody component whereas the LF and BE spectra were fit with a simple power-law model. The hydrogen column density was fixed to $N_H = 5.6 \times 10^{21} \text{ cm}^{-2}$ (Falanga et al. 2005a). The resulting fit parameters are presented in Table B3.

B4 NGC 6440 X-2:

For ObsIDs 94044-04-02-00 and 96326-01-36-00 data was extracted from PCU2 whereas for ObsID 96326-01-40-01 data was taken from PCU 1 and 2. The hydrogen column density was fixed to $N_H = 5.9 \times 10^{21} \text{ cm}^{-2}$ (Harris 1996). The data were fit with a simple absorbed power-law for all ObsIDs. The fit parameters are presented in Table B4.

B5 IGR J17511–3057:

For ObsID 94041-01-01-02 (HF) the data were extracted from PCU 2. For ObsIDs 94042-01-03-04 (LF) and 94042-01-02-05 (BE) spectral analysis was performed by combining data from PCUs 2, 3 and PCUs 2, 4 respectively. The hydrogen column density was fixed to $N_H = 1 \times 10^{22} \text{ cm}^{-2}$ (Papitto et al. 2010; Paizis et al. 2012). The HF was well described with a power-law continuum and thermal blackbody component, whereas the LF and BE spectra were fit with a simple absorbed power law. A Gaussian feature at ~ 6.5 keV was added to the HF and BE spectra to improve the fits. The resulting parameters are presented in Table B5.

B6 XTE J1814–338:

Since the observed count rate of XTE J1814–338 is small ($< 40 \text{ ct s}^{-1}$ for the entire outburst), data from all available PCUs were combined for all spectra. For ObsID 80418-01-03-08 (HF) the data were extracted from PCU 0, 2 and 3. For 80418-01-07-08 (LF) data from PCUs 0, 1, 2 and 3 and for 80418-01-09-00 (BE) PCUs 0, 1 and 2 were used. The hydrogen column density was fixed to $N_H = 1.67 \times 10^{21} \text{ cm}^{-2}$ (Krauss et al. 2005b).

The HF spectrum was fit with a power-law continuum and a blackbody component, whereas the LF and BE spectra were fit with a simple absorbed power-law model. The details of the fit parameters are presented in Table B6.

B7 HETE J1900.1–2455:

The data were extracted from all layers of PCU2 for the considered ObsIDs. The hydrogen column density was fixed to $N_H = 1 \times 10^{21} \text{ cm}^{-2}$ (Papitto et al. 2013a). We obtain the HF spectrum from ObsID 91015-01-06-00 with fit with *tbabs*cutoffpl*. We found a large excess at ~ 6 keV, which was modelled with a Gaussian centred at ~ 6.2 keV with a width of ~ 1 keV. The resulting fits were statistically acceptable.

The ObsID 91059-03-02-00 (LF) was fit with *tbabs(bbody+powerlaw)*. A weak Gaussian feature at ~ 6.5 keV was added to improve the fits. The results are presented in Table B7.

A background estimate is not available for this source.

Table B1. Spectral fit parameters of Swift J1756.9–2508.

| | High flux | Swift J1756.9–2508 | |
|---|---------------------------------|-----------------------------------|---------------------------------|
| | | Low flux | Background |
| ObsIDs | 94065-02-01-05 | 94065-06-02-03 | 94065-06-03-02 |
| $N_H(10^{22} \text{ cm}^{-2})$ | 5.4 (fixed) | 5.4 (fixed) | 5.4 (fixed) |
| T_{BB} (keV) | – | 0.49 ± 0.08 | – |
| Norm _{bb} | – | $10^{+6}_{-2} \times 10^{-4}$ | – |
| Γ | 1.970 ± 0.014 | 2.24 ± 0.06 | 2.67 ± 0.11 |
| $\chi^2/\text{d.o.f.}$ | 45.66/37 | 40.39/41 | 34.68/36 |
| Flux (erg cm ⁻² s ⁻¹) | $6.30 \pm 0.04 \times 10^{-10}$ | $1.990 \pm 0.017 \times 10^{-10}$ | $4.07 \pm 0.15 \times 10^{-11}$ |

N_H is the column density of neutral hydrogen for the *tbabs* model, T_{bb} is the black body temperature, Norm_{bb} is the normalisation of the *bbody* model, Γ is the power-law index. The first column represents the highest flux (HF) with pulsations, the second column gives the lowest flux (LF) with pulsations and the third column gives the observation used to measure the background emission (BE).

Table B2. Spectral fit parameters of XTE J0929–314, see Table B1 for details.

| | High flux | XTE J0929–314 | |
|---|---------------------------------|---------------------------------|------------|
| | | Low flux | Background |
| ObsIDs | 70096-03-02-00 | 70096-03-14-00 | – |
| $N_H(10^{22} \text{ cm}^{-2})$ | 0.0076 (fixed) | 0.0076 (fixed) | – |
| T_{BB} (keV) | 0.82 ± 0.04 | 0.53 ± 0.05 | – |
| Norm _{bb} | $3.5 \pm 0.5 \times 10^{-3}$ | $1.9 \pm 0.4 \times 10^{-3}$ | – |
| Γ | 1.80 ± 0.04 | 1.90 ± 0.11 | – |
| $\chi^2/\text{d.o.f.}$ | 36.33/42 | 26.11/42 | – |
| Flux (erg cm ⁻² s ⁻¹) | $4.42 \pm 0.02 \times 10^{-10}$ | $6.64 \pm 0.14 \times 10^{-11}$ | – |

B8 SAX J1808.4–3658:

For ObsID 70080-01-01-04 (HF) the data were extracted from the top layers of PCU2. The hydrogen column density was fixed to $N_H = 2 \times 10^{21} \text{ cm}^{-2}$ (Papitto et al. 2009; Cackett et al. 2009; Patruno et al. 2009c). The continuum was modelled with the thermal comptonisation *NTHCOMP* of Zdziarski et al. (1996); Życki et al. (1999). A blackbody and diskblackbody component were also required to model the continuum. A broad excess at ~ 6.2 keV was seen in the residuals, reminiscent of a relativistically broadened iron line reported in other works (Papitto et al. 2009; Patruno et al. 2009c; Cackett et al. 2009). However, owing to the poor spectral resolution of RXTE, we have not employed the sophisticated relativistic models like *diskline* and instead modelled the feature with a broadened Gaussian. The central energy of the Gaussian was fixed to 6.2 keV.

Data for ObsIDs 30411-01-11-00 (LF) and 30411-01-11-02 (BE) was extracted from all PCUs and combined for spectral analysis. The data fit well with a simple power-law model. The results are presented in Table B8.

B9 IGR J17498–2921:

Data for all ObsIDs viz. 96435-01-02-01 (HF), 96435-01-06-04 (LF) and 96435-01-07-01 (BE) were extracted from all layers of PCU 2. All three spectra were fit with a simple power-law continuum model and a thermal blackbody com-

ponent. A narrow Gaussian component centred at ~ 6.5 keV (most likely a feature from background emission) was required to obtain a statistically acceptable fit. The hydrogen column density was fixed to $N_H = 2.87 \times 10^{22} \text{ cm}^{-2}$ (Torres et al. 2011). The results are presented in Table B9.

We note that flux measured from the LF and BE observations are the same within error, indicating that the lowest flux with pulsations is background dominated.

B10 XTE J1751–305:

For all ObsIDs viz. 70131-03-01-00 (HF), 70131-01-09-000 (LF) and 70131-02-04-00 (BE), data was extracted from PCU2. For the HF and BE, the spectra were fit with *tbabs(powerlaw+bbbody)*. The LF spectrum was fit with a simple absorbed powerlaw. Additionally, a narrow Gaussian component centred at ~ 6.5 keV was required for the low flux observations. The neutral hydrogen column density was fixed to $N_H = 1 \times 10^{22} \text{ cm}^{-2}$ (Miller et al. 2003; Gierliński & Poutanen 2005). The results are presented in Table B10.

B11 SAX J1748.9–2021:

For ObsID 94315-01-06-07 (HF) and 60035-02-03-02 (LF) the data were extracted from PCU 2, whereas for 94315-01-11-02 (BE) the combined spectra from PCU 0 and 2 were used. The HF and LF spectra fit with *tbabs(bbody+cutoffpl)*.

Table B3. Spectral fit parameters of XTE J1807.4–294, see Table B1 for details.

| | XTE J1807.4–294 | | |
|---|---------------------------------|---------------------------------|---------------------------------|
| | High flux | Low flux | Background |
| ObsIDs | 70134-09-02-01 | 80145-01-17-02 | 80419-01-01-01 |
| $N_H(10^{22} \text{ cm}^{-2})$ | 0.56 (fixed) | 0.56 (fixed) | 0.56 (fixed) |
| Γ | 1.90 ± 0.03 | 2.19 ± 0.04 | 2.16 ± 0.04 |
| T_{BB} (keV) | $1.46^{+0.33}_{-0.19}$ | – | – |
| Norm _{bb} | $4.9 \pm 0.2 \times 10^{-4}$ | – | – |
| $\chi^2/\text{d.o.f.}$ | 49.87/42 | 31.07/44 | 34.69/44 |
| Flux (erg cm ^{−2} s ^{−1}) | $8.19 \pm 0.04 \times 10^{-10}$ | $3.51 \pm 0.07 \times 10^{-10}$ | $7.25 \pm 0.15 \times 10^{-11}$ |

Table B4. Spectral fit parameters of NGC 6440 X-2, see Table B1 for details.

| | NGC 6440 X-2 | | |
|---|---------------------------------|-------------------------------|-------------------------------|
| | High flux | Low flux | Background |
| ObsIDs | 94044-04-02-00 | 96326-01-40-01 | 96326-01-36-00 |
| $N_H(10^{22} \text{ cm}^{-2})$ | 0.59 (fixed) | 0.59 (fixed) | 0.59 (fixed) |
| Γ | 1.83 ± 0.02 | $2.36^{+0.21}_{-0.12}$ | 2.3 ± 0.4 |
| Γ (Cutoffpl) | – | 1.1 ± 0.8 | – |
| E_{cut} | – | 5.5^{+9}_{-2} | – |
| $\chi^2/\text{d.o.f.}$ | 34.38/38 | 45/35 | 36.77/44 |
| Flux (erg cm ^{−2} s ^{−1}) | $2.62 \pm 0.03 \times 10^{-10}$ | $3.4 \pm 0.2 \times 10^{-11}$ | $1.3 \pm 0.2 \times 10^{-11}$ |

E_{cut} is the high energy cutoff for a cutoff power-law model.

Table B5. Spectral fit parameters of IGR J17511–3057, see Table B1 for details.

| | IGR J17511–3057 | | |
|---|---------------------------------|-----------------------------------|-----------------------------------|
| | High flux | Low flux | Background |
| ObsIDs | 94041-01-01-02 | 94042-01-03-04 | 94042-01-02-05 |
| $N_H \times 10^{22} \text{ cm}^{-2}$ | 1 (fixed) | 1 (fixed) | 1 (fixed) |
| T_{BB} (keV) | 1.10 ± 0.16 | – | – |
| Norm _{bb} | $6 \pm 3 \times 10^{-4}$ | – | – |
| Γ | 1.70 ± 0.04 | 2.02 ± 0.04 | 2.37 ± 0.06 |
| $\chi^2/\text{d.o.f.}$ | 44.81/39 | 39.89/41 | 36.71/44 |
| Flux (erg cm ^{−2} s ^{−1}) | $8.65 \pm 0.05 \times 10^{-10}$ | $1.000 \pm 0.018 \times 10^{-10}$ | $6.960 \pm 0.018 \times 10^{-11}$ |

Table B6. Spectral fit parameters of XTE J1814–338, see Table B1 for details.

| | XTE J1814–338 | | |
|---|---------------------------------|---------------------------------|---------------------------------|
| | High flux | Low flux | Background |
| ObsIDs | 80418-01-03-08 | 80418-01-07-08 | 80418-01-09-00 |
| $N_H(10^{22} \text{ cm}^{-2})$ | 0.167 (fixed) | 0.167 (fixed) | 0.167 (fixed) |
| T_{BB} (keV) | 1.21 ± 0.06 | – | – |
| Norm _{bb} | $1.7 \pm 0.4 \times 10^{-3}$ | – | – |
| Γ | 1.55 ± 0.04 | 1.96 ± 0.03 | 2.4 ± 0.3 |
| $\Delta\chi^2/\text{d.o.f.}$ | 63.99/42 | 23.2/43 | 28.17/44 |
| Flux (erg cm ^{−2} s ^{−1}) | $4.41 \pm 0.03 \times 10^{-10}$ | $6.00 \pm 0.10 \times 10^{-11}$ | $1.00 \pm 0.16 \times 10^{-11}$ |

Table B7. Spectral fit parameters of HETE J1900.1–2455, see text and Table B1 for further details.

| | HETE J1900.1–2455 | | |
|-----------------------------------|--------------------------------|---------------------------------|------------|
| | High flux | Low flux | Background |
| ObsIDs | 91015-01-06-00 | 91059-03-02-00 | – |
| $N_H(10^{22} \text{ cm}^{-2})$ | 0.1 (fixed) | 0.1 (fixed) | – |
| T_{BB} (keV) | | 0.74 ± 0.10 | – |
| Norm_{bb} | | $8 \pm 2 \times 10^{-4}$ | – |
| Γ (cutoffpl) | 0.9 ± 0.1 | | – |
| E_{cut} | 4.0 ± 0.2 | | – |
| Γ | | 1.83 ± 0.07 | – |
| $\chi^2/\text{d.o.f.}$ | 42.74/40 | 25.26/40 | – |
| Flux (erg cm $^{-2}$ s $^{-1}$) | $1.15 \pm 0.05 \times 10^{-9}$ | $3.84 \pm 0.03 \times 10^{-10}$ | – |

Table B8. Spectral fit parameters of SAX J1808.4–3658.

| | SAX J1808.4–3658 | | |
|-----------------------------------|----------------------------------|---------------------------------|---------------------------------|
| | High flux | Low flux | Background |
| ObsIDs | 70080-01-01-04 | 30411-01-11-00 | 30411-01-11-02 |
| $N_H(10^{22} \text{ cm}^{-2})$ | 0.2 (fixed) | 0.2 (fixed) | 0.2 (fixed) |
| Γ (Powerlaw) | – | 2.24 ± 0.05 | 2.23 ± 0.11 |
| T_{bb} (keV) | 1.25 ± 0.07 | – | – |
| Norm_{bb} | $9.2 \pm 1.4 \times 10^{-3}$ | – | – |
| T_{disk} (keV) | 0.45 ± 0.06 | – | – |
| $\text{Norm}_{\text{disk}}$ | $8.7^{+18}_{-5} \times 10^3$ | – | – |
| E_1 (keV) | 6.2 (fixed) | – | – |
| σ_1 (keV) | 1.04 ± 0.15 | – | – |
| Γ (NTHCOMP) | 2.3 ± 0.1 | – | – |
| T_e (keV) | 100 (fixed) | – | – |
| $\chi^2/\text{d.o.f.}$ | 33.37/35 | 50.18/45 | 35.47/43 |
| Flux (erg cm $^{-2}$ s $^{-1}$) | $1.850 \pm 0.007 \times 10^{-9}$ | $2.82 \pm 0.07 \times 10^{-11}$ | $1.21 \pm 0.08 \times 10^{-11}$ |

T_{disk} is the temperature of the inner radius of the accretion disk, and $\text{Norm}_{\text{disk}}$ is the normalisation of the *diskbb* model. The fluorescent iron line is fit with a Gaussian component, such that E_1 is the line energy and σ_1 the width of the line. Similarly E_2 and σ_2 are the line energy and width of a Gaussian component needed to model an excess at ~ 5.4 keV. See text and Table B1 for further details.

Table B9. Spectral fit parameters of IGR J17498–2921, see Table B1 for details.

| | IGR J17498–2921 | | |
|-----------------------------------|--|--------------------------------------|---------------------------------|
| | High flux | Low flux | Background |
| ObsIDs | 96435-01-02-01 | 96435-01-06-04 | 96435-01-07-01 |
| $N_H(10^{22} \text{ cm}^{-2})$ | 2.87 (fixed) | 2.87 (fixed) | 2.87 (fixed) |
| T_{BB} (keV) | 1.51 ± 0.05 | 1.93 ± 0.15 | 1.76 ± 0.08 |
| Norm_{bb} | $1.9 \pm 0.2 \times 10^{-3}$ | $1.41^{+0.2}_{-0.08} \times 10^{-3}$ | $2.2 \pm 0.2 \times 10^{-3}$ |
| Γ | 1.93 ± 0.02 | $2.39^{+0.1}_{-0.06}$ | 2.3 ± 0.1 |
| $\chi^2/\text{d.o.f.}$ | 52.76/39 | 28.90/38 | 32.39/38 |
| Flux (erg cm $^{-2}$ s $^{-1}$) | $1.130^{+0.003}_{-0.006} \times 10^{-9}$ | $4.44 \pm 0.04 \times 10^{-10}$ | $4.23 \pm 0.04 \times 10^{-10}$ |

Table B10. Spectral fit parameters of XTE J1751–305, see Table B1 for details.

| | XTE J1751–305 | | |
|-----------------------------------|---|---------------------------------|---------------------------------|
| | High flux | Low flux | Background |
| ObsIDs | 70134-03-01-00 | 70131-01-09-000 | 70131-02-04-00 |
| $N_H (10^{22} \text{ cm}^{-2})$ | 1 (fixed) | 1 (fixed) | 1 (fixed) |
| T_{bb} (keV) | 1.95 ± 0.16 | – | – |
| Norm_{bb} | $2.1 \pm 0.3 \times 10^{-3}$ | – | – |
| T_{disk} (keV) | – | – | – |
| $\text{Norm}_{\text{disk}}$ | – | – | – |
| Γ | 1.77 ± 0.03 | 2.070 ± 0.007 | 2.32 ± 0.03 |
| $\chi^2/\text{d.o.f.}$ | 47.59/40 | 38.07/35 | 56.08/40 |
| Flux (erg cm $^{-2}$ s $^{-1}$) | $1.500^{+0.006}_{-0.01} \times 10^{-9}$ | $3.97 \pm 0.01 \times 10^{-10}$ | $6.51 \pm 0.08 \times 10^{-11}$ |

Table B11. Spectral fit parameters of SAX J1748.9–2021, see Table B1 for details.

| | SAX J1748.9–2021 | | |
|-----------------------------------|--------------------------------|------------------------------------|-------------------------------|
| | High flux | Low flux | Background |
| ObsIDs | 94315-01-06-07 | 60035-02-03-02 | 94315-01-11-02 |
| $N_H (10^{22} \text{ cm}^{-2})$ | 0.59 (fixed) | 0.59 (fixed) | 0.59 (fixed) |
| T_{bb} (keV) | 2.11 ± 0.14 | $0.63^{+0.06}_{-0.11}$ | – |
| Norm_{bb} | $1.30 \pm 0.19 \times 10^{-2}$ | $6.5^{+2.9}_{-1.7} \times 10^{-3}$ | – |
| Γ (cutoffpl) | 1.00 ± 0.16 | $0.39^{+0.15}_{-0.23}$ | – |
| E_{cut} (keV) | 4.1 ± 0.6 | $3.36^{+0.16}_{-0.21}$ | – |
| Γ (power law) | – | – | 2.2 ± 0.2 |
| $\chi^2/\text{d.o.f.}$ | 45.41/41 | 36.21/33 | 28.23/43 |
| Flux (erg cm $^{-2}$ s $^{-1}$) | $4.13 \pm 0.01 \times 10^{-9}$ | $2.960 \pm 0.005 \times 10^{-9}$ | $1.9 \pm 0.2 \times 10^{-11}$ |

The BE spectrum was fit using an absorbed power-law. The hydrogen column density was fixed to $N_H = 5.9 \times 10^{21} \text{ cm}^{-2}$ (Harris 1996). A Gaussian emission feature centred at ~ 6.5 keV was used to improve statistics of the LF spectrum fit. The results are presented in Table B11.

B12 Swift J1749.4–2807:

The data were extracted from PCU2 for all ObsIDs (HF: 95085-09-01-00, LF: 95085-09-02-07, BE: 95085-09-02-10). There was an eclipse during the observation in 95085-09-01-00 (Markwardt & Strohmayer 2010; Ferrigno et al. 2011), so for the spectral analysis of that observation we considered only the data from the initial 990 s when the source was visible. The spectra were fit with power-law continuum model. The neutral hydrogen column density was fixed to $N_H = 3 \times 10^{22} \text{ cm}^{-2}$ (Ferrigno et al. 2011; Wijnands et al. 2009). For the LF and BE an additional blackbody component was required. The results are presented in Table B12.

B13 Aql X-1:

Since the pulsations of Aql X-1 have been detected only once (ObsID 30188-03-05-00), we use this observation as both the HF and LF. We extract the data from PCU2 and fit

the spectrum with a *tbabs(cutoffpl+Gaussian+bbody)* model. The background emission is evaluated from ObsID 30073-06-01-00, which was fit with a simple absorbed power-law. Our results are shown in Table B13.

B14 IGR J00291+5934:

For the ObsID 90052-03-01-00 (HF) data from PCU2 were used for spectral analysis. For 90425-01-02-01 (LF) and 90425-01-03-06 (BE) data from all active PCUs (PCU 0, 2 and PCU 0, 2, 3 respectively) were combined to improve the photon statistics.

The HF spectrum was fit with the thermal blackbody and power-law models. The LF and BE spectra were fit with a simple absorbed power law. The neutral hydrogen column density was fixed to $N_H = 0.46 \times 10^{22} \text{ cm}^{-2}$ based on measurements from *XMM-Newton* and *Chandra* observations (Torres et al. 2008; Paizis et al. 2005). A gaussian emission feature was required to improve the fits of the LF and BE spectra. The fit results are given in Table B14.

Table B12. Spectral fit parameters of Swift J1749.4–2807, see Table B1 for details.

| | Swift J1749.4–2807 | | |
|---|---------------------------------|---------------------------------|---------------------------------|
| | High flux | Low flux | Background |
| ObsIDs | 95085-09-01-00 | 95085-09-02-05 | 95085-09-02-10 |
| $N_H(10^{22} \text{ cm}^{-2})$ | 3 (fixed) | 3 (fixed) | 3 (fixed) |
| T_{bb} (keV) | – | 1.67 ± 0.11 | 1.8 ± 0.2 |
| Norm _{bb} | – | $7.94 \pm 1.2 \times 10^{-4}$ | $5.8 \pm 1.2 \times 10^{-4}$ |
| Γ | 1.89 ± 0.02 | 1.78 ± 0.08 | 1.90 ± 0.09 |
| $\chi^2/\text{d.o.f.}$ | 43.21/41 | 54.01/33 | 39.77/39 |
| Flux (erg cm ^{−2} s ^{−1}) | $5.24 \pm 0.06 \times 10^{-10}$ | $2.67 \pm 0.02 \times 10^{-10}$ | $2.41 \pm 0.03 \times 10^{-10}$ |

Table B13. Spectral fit parameters of Aql X-1, see Table B1 for details.

| | Aql X-1 | |
|---|--------------------------------|---------------------------------|
| | High/Low flux | Background |
| ObsIDs | 30188-03-05-00 | 30073-06-01-00 |
| $N_H(10^{22} \text{ cm}^{-2})$ | 0.4 (fixed) | 0.4 (fixed) |
| T_{bb} (keV) | $0.81^{+0.44}_{-0.09}$ | – |
| Norm _{bb} | $1.2^{+2.1}_{-0.6}$ | – |
| Γ | – | 1.92 ± 0.02 |
| Γ (cutoffpl) | $0.7^{+0.2}_{-0.4}$ | – |
| E_{cut} (keV) | 3.4 ± 0.4 | – |
| E_1 (keV) | $6.32^{+0.18}_{-0.38}$ | – |
| σ_1 (keV) | 1.0 ± 0.3 | – |
| $\chi^2/\text{d.o.f.}$ | 45.95/38 | 45.39/43 |
| Flux (erg cm ^{−2} s ^{−1}) | $8.74 \pm 0.01 \times 10^{-9}$ | $1.34 \pm 0.05 \times 10^{-11}$ |

Table B14. Fit parameters from spectral analysis of IGR J00291+5934.

| | IGR J00291+5934 | | |
|---|--------------------------------|---------------------------------|---------------------------------|
| | High flux | Low flux | Background |
| ObsIDs | 90052-03-01-00 | 90425-01-02-01 | 90425-01-03-06 |
| $N_H(10^{22} \text{ cm}^{-2})$ | 0.46 (fixed) | 0.46 (fixed) | 0.46 (fixed) |
| Γ | 1.50 ± 0.04 | 1.73 ± 0.04 | 1.50 ± 0.03 |
| T_{BB} (keV) | 1.14 ± 0.06 | – | – |
| Norm _{bb} | $1.05 \pm 0.03 \times 10^{-3}$ | – | – |
| $\chi^2/\text{d.o.f.}$ | 48.81/42 | 22.92/35 | 30.55/41 |
| Flux (erg cm ^{−2} s ^{−1}) | $9.7 \pm 0.05 \times 10^{-10}$ | $1.09 \pm 0.02 \times 10^{-10}$ | $5.76 \pm 0.09 \times 10^{-11}$ |